

Full-Aircraft Energy-Based Force Decomposition Applied to Boundary Layer Ingestion

Drewan S. Sanders* and Panagiotis Laskaridis†
Cranfield University, Cranfield, Bedfordshire, MK43 0AL, United Kingdom

This paper introduces a generic force decomposition method derived from mechanical energy conservation. A transformation from relative to absolute reference frame captures the power transfer from pressure and skin-friction forces on aircraft surfaces to mechanisms in the flow-field. A unique flow-feature extraction procedure isolates these mechanisms into different regions including the jet-plume substructures, as well as shocks and shear-layers located externally to the jet. Featured is a novel shear-layer identification metric that captures both laminar and turbulent regions. The resulting energy balance is rearranged into a force decomposition formulation with contributions attributed to shocks, jets, lift induced vortices and the remaining wake. Boundary layer ingestion is used to demonstrate the method where a Potential for Energy Recovery factor is introduced and defines the amount of energy available at the trailing edge of an unpowered body. CFD results of a fuselage suggest 10% of its drag power is available for re-utilisation. CFD studies of a boundary layer ingesting propulsor show local minima in power consumption at a given thrust-split for particular combinations of fan pressure ratio and amount of boundary layer ingested. A noteworthy finding reveals significant contributions of volumetric pressure work, a term often neglected in previous work.

Nomenclature

ARF	=	Absolute Reference Frame
A_i, A_{th}	=	intake highlight and throat areas [m ²]
$A_{fan,i}, A_{fan,o}$	=	fan inlet and outlet areas [m ²]
A_{noz}	=	nozzle exit area [m ²]
BLR	=	boundary layer ingestion ratio [%], $(\dot{m}/\dot{m}_{BL,ref})$
C_X	=	power coefficients for \dot{E} , Θ and Φ [-], $\left(X/\left[\frac{1}{2}\rho_\infty V_\infty^3 S_{ref}\right]\right)$
Δc	=	intake centreline offset [m]
$d_{farfield}, d_{outlet}$	=	distance from body to CFD domain's far-field and outlet boundary conditions, respectively

*Research Fellow, School of Aerospace, Transport and Manufacturing, d.s.sanders@cranfield.ac.uk

†Senior Lecturer, School of Aerospace, Transport and Manufacturing

d_{FP}, d_{SC}, d_{TP}	= distance from body to control volume front plane, side cylinder and Trefftz plane, respectively
$\overline{\underline{d}}$	= deviatoric stress tensor
\dot{E}_a	= streamwise kinetic energy flux via Trefftz plane [W]
\dot{E}_p	= rate of pressure boundary work on Trefftz plane [W]
\dot{E}_τ	= rate of viscous boundary work on Trefftz plane [W]
\dot{E}_v	= transverse kinetic energy flux via Trefftz plane [W]
\dot{E}	= total mechanical energy flux in the ARF [W]
\dot{E}_k	= kinetic energy flux in the ARF [W]
\dot{E}_p	= rate of pressure boundary work in the ARF [W]
\dot{E}_{prop}	= propulsor power flux [W]
\dot{E}_τ	= rate of viscous boundary work in the ARF [W]
e	= mass specific internal energy [J/kg]
e_a^{21}	= grid convergence approximate relative error [%]
e_{ext}^{21}	= grid convergence extrapolated relative error [%]
\mathbf{F}	= force vector [N]
\mathbf{F}_B	= integrated force acting on the body's surfaces by the fluid [N]
\mathbf{F}_{iso}	= non-aerodynamic force opposing \mathbf{F}_N to maintain equilibrium [N]
\mathbf{F}_N	= net aerodynamic force [N]
$F_{Nx,ref}$	= reference net assembly thrust [N]
FPR	= fan pressure ratio [-]
\mathbf{f}	= volume specific body force vector [N/m ³]
g	= gravitational acceleration [m/s ²]
GCI_{fine}^{21}	= fine Grid Convergence Index [%]
H	= total enthalpy [J/kg]
\dot{h}	= rate of change in altitude [m/s]
$\overline{\underline{I}}$	= second order tensor identity matrix
k	= turbulent kinetic energy [J/kg]
\mathcal{K}	= thermal conductivity [W/(m·K)]
$l_{fuse}, l_{nose}, l_{tail}$	= fuselage overall, nose and tail lengths, respectively. [m]
$l_{intake}, l_{fan}, l_{exhaust}$	= nacelle intake, fan and exhaust lengths, respectively. [m]
m	= mass [kg]
\dot{m}	= mass flow rate [kg/s]

\hat{n}	=	unit normal vector
N_1, N_2, N_3	=	number of cells in grid refinement volume [-]
PER	=	Potential for Energy Recovery [%]
p	=	static pressure [Pa]
p_G	=	gauge static pressure $p - p_\infty$ [Pa]
p	=	grid convergence apparent order [-]
\dot{q}	=	volumetric heat addition/removal [J/(kg · s)]
\mathbf{q}	=	heat conduction flux vector [J/(kg · s)]
r_{21}, r_{32}	=	medium-to-fine and coarse-to-medium grid refinement factors [-]
r_{tail}	=	radius of arc connecting the midsection to the tail-cone of the fuselage [m]
$r_{\text{noz,i}}, r_{\text{noz,o}}$	=	nozzle internal inner & outer radius [m]
r_{aft}	=	radius the nacelle after-body [m]
R_{fuse}	=	radius of fuselage's cylindrical midsection [m]
$\overline{\overline{R}}$	=	Reynolds stress tensor
RRF	=	Relative Reference Frame
$\overline{\overline{S}}$	=	rate-of-strain tensor
\mathcal{S}	=	control volume surface
$d\mathcal{S}$	=	infinitesimal surface vector area [m ²], ($\hat{n} d\mathcal{S}$)
T	=	static temperature [K]
u, v, w	=	velocity components in the absolute reference frame [m/s]
\mathbf{V}	=	velocity vector relative to the aircraft [m/s], ($\mathbf{V}_A + \mathbf{V}_\infty$)
\mathbf{V}_A	=	absolute velocity vector in reference to the earth [m/s], ($\mathbf{V} - \mathbf{V}_\infty$)
\mathbf{V}_B	=	aircraft flight velocity in reference to the earth [m/s], ($\mathbf{V} - \mathbf{V}_\infty$)
\mathbf{V}_e	=	shear layer edge velocity [m/s]
\mathbf{V}^2	=	$\mathbf{V} \cdot \mathbf{V}$
\mathcal{V}	=	control volume [N/m ³]
\mathcal{V}_P	=	propulsor control volume [N/m ³]
$d\mathcal{V}$	=	infinitesimal control volume [m ³]
\dot{W}_P	=	BLI propulsor shaft power [W]
β	=	tail-cone's trailing edge angle [rad]
β_1	=	nacelle orientation angle [rad]
$\beta_{\text{hade,i}}, \beta_{\text{hade,o}}$	=	fan casing inner & outer hade angles [rad]

β_{noz}	=	nozzle exit angle [rad]
γ	=	flight climb/descent angle [rad]
δ	=	boundary layer thickness [m]
ξ	=	volumetric shock filter metric [-]
Θ	=	rate of volumetric pressure work [W]
κ	=	$F_{x,\text{ref}} \cdot V_{\infty} / \dot{W}_P$
μ	=	laminar dynamic viscosity [N·s/m ²]
μ_t	=	turbulent viscosity [N·s/m ²]
ζ	=	volumetric shear layer filter metric [-]
ρ	=	density [kg/m ³]
$\overline{\overline{\tau}}$	=	viscous stress tensor [Pa]
$\vec{\tau}$	=	viscous stress vector [Pa], $\left(\overline{\overline{\tau}} \cdot \hat{n}\right)$
Υ	=	volumetric jet plume filter metric [-]
ϕ_1, ϕ_2, ϕ_3	=	unpowered body force coefficient for fine, medium & coarse grids [m ²]
ϕ_{ext}^{21}	=	extrapolated unpowered body force coefficient [m ²]
Φ	=	rate of volumetric viscous dissipation [W]
Φ^*	=	total power transfer for a control volume [W], Eq. (24)
Subscripts		
B	=	forces and surfaces of the airframe body
BL	=	boundary layer
O	=	outer control volume surface
P	=	forces and surfaces of the propulsor
ref	=	reference aircraft/fuselage
SC	=	side cylinder
TE	=	trailing edge
TP	=	Trefftz plane
iso	=	isolated from flow-field
vortex	=	lift induced vortex
∞	=	freestream

I. Introduction

MOMENTUM conservation allows for calculation of net aircraft forces from either integration of pressure and skin friction forces along all physical surfaces, or alternatively from integration of momentum fluxes through control volume surfaces encapsulating the aircraft. The former and latter may be referred to as near and far-field approaches, respectively, although differences in definitions may vary [1–6]. Near-field integration is limiting, as it only allows for drag decomposition into pressure and skin friction components. This has further limitations where the airframe and propulsion system cannot be aerodynamically decoupled, because of the difficulty in defining what is thrust versus drag [7–10] before distinguishing between pressure and skin friction components. The more aerodynamically integrated the airframe and propulsion system, the more difficult it becomes to make use of near-field integration methods to yield anything more than a net force on the overall vehicle. As a result, conventional methods of thrust-drag bookkeeping [11, 12] are of little use, because it is not possible to work within the formal definition of drag, which requires the subtraction of pressure forces in potential flow from the forces in real flow. Instead for extreme cases such as BLI, alternative definitions of thrust-*force* accounting have been introduced and explored [13]. Although these alternatives provide a means for conveniently separating thrust and force, they are unable to decompose these into meaningful contributions like profile, lift-induced, wave and jet constituents. Additionally, the separation of thrust from force is based on a notional definition, and thus there is no clear way to translate thrust to useful work, which is usually the numerator of classical propulsive efficiency definition. Or conversely, there is no way to meaningfully represent useful work indirectly as a thrust. This inadequacy of the propulsive efficiency definition not only applies to unconventional configurations, but extends to traditional propulsion installations too, as it only truly works for a strictly ideal case where propulsor and airframe (including nacelles / shrouds) may be perfectly decoupled. This observation opens up a larger debate into how combined airframe-propulsion aerodynamic efficacy may be understood, quantified and compared. To begin tackling some of these questions, it is a good starting point to examine how aircraft net forces may be decomposed.

Control volume approaches to drag estimation and decomposition have been explored in references [1, 2, 4–6, 14], where perturbation velocities in the momentum equation are substituted by manipulated forms of stagnation entropy and enthalpy definitions. As such, it is possible to derive surface integrals of the aircraft wake in which entropy terms correspond to profile, wave, lift-induced vortex and interference drag, whereas enthalpy terms are associated with thrust [1]. Alternatively, Gauss’ Theorem allows for these terms to be expressed as volume integrals, which means that drag and thrust components may be attributed to local physical mechanisms within the flow-field surrounding the aircraft. This requires identifying and separating out regions of the flow containing shear layers, shocks, vortices and jets; the volume integrals of which then correspond to profile drag, wave drag, induced drag and thrust, respectively. Such an approach, along with regional selectors, has been formulated for CFD post-processing by Paparone and Tognaccini [2], with further considerations given to power-on conditions [15]. An additional apparent advantage, is the use of

entropy volume integrals to compute and exclude some of the numerically generated spurious drag to improve drag prediction accuracy. This method has been applied to the NASA Common Research Model during the 4th Drag Prediction Workshop, to demonstrate its capabilities for full-aircraft drag estimation and decomposition in unpowered conditions [16]. Despite the usefulness of the above, the mathematical terms are complex, lack physical intuitiveness and are typically reliant on Taylor series expansion, thereby neglecting higher order terms. Additionally, it must be noted, as in the case of other volume integral approaches [4–6], that wake surface integrals were used to approximate lift-induced drag, the complexities of which are discussed in detail by Spalart [17] who calls into question the rigour to which lift-induced drag may be defined.

A promising approach to addressing the lift induced drag decomposition challenge, is through the use of vortex force methods [3, 18–21]. In primarily tackling the difficulty of applying entropy-based decomposition methods to unsteady flows, Marongiu and Tognaccini [22] adopted the theory of Wu [23] and Wu et al. [24] to develop an alternative decomposition method which is based around the vortex force associated with integrals of the Lamb vector. The initial work extended the incompressible approach to a RANS formulation, such that it could be applied to high Reynolds number flows, resulting in a decomposition of lift from drag with each containing terms of both surface and volume integrals. However, an important advantage of the vortex force approach, is that it enables the unambiguous calculation of lift-induced drag from numerical solutions [18], thereby providing a more rigorous definition in response to Spalart’s [17] concerns whilst avoiding the difficulties of Trefftz plane positioning in entropy-based methods because of rapid vortex decay downstream of the aircraft. Subsequently, further development saw the inclusion of compressibility correction term, which allowed for full decomposition of lift from drag with its wave, profile and lift-induced components in 2D and 3D flows [3, 19–21]. Although vortex force methods appear to provide an elegant solution to lift-induced drag calculations and have been applied to wing-body configurations, they have not yet been developed for full-aircraft decompositions where the propulsion system is included within the flow domain and interacts aerodynamically with the airframe. This is an important aspect as aircraft design moves toward more integrated installations in an ambition to reduce fuel consumption.

Drela’s approach [7], although intended for overcoming thrust-drag accounting definition problems for tightly integrated airframe-propulsion systems, addresses some issues of entropy-based and vortex force methods through a control volume formulation of the mechanical energy equation. Here, aircraft aerodynamics are described as a balance between power inflows and outflows, which are decomposed into physically intuitive forms. The decomposition includes powers correlating to profile drag, induced drag, wave drag and jet components. The use of power instead of entropy terms, allows for improved interpretation through the way in which mathematical terms are easily related back to different forms of energy. One example is in isolating lift-induced drag where, the physical interpretation enabled by the overall power balance clarifies the pressure work behind a debated negative streamwise kinetic energy term within the induced drag surface integral across the wake. Although still subject to the same Trefftz plane position

difficulties as the entropy-based methods, the improved interpretation does address this concern of Spalart [17]. The advantage the power balance method has over the vortex force approaches above, is that it is readily applicable to powered configurations, allowing for the energetic contributions of the propulsion system to be included within the power decomposition. Arntz et al. [25] developed a similar approach, which considers an exergy assessment of the total energy equation, thereby introducing additional terms from the first and second laws of thermodynamics. Exergy may prove useful in providing a global metric for analysing full aircraft performance analysis [26] however, although more complete, the exergy formulation simplifies down to the same equation as Drela's power balance method under typical assumptions neglecting heat transfer in external aerodynamics. Therefore, the two approaches are regarded as being equivalent, as the semantics of exergy and anergy are synonymous with the power terms defined by Drela. Based on this review, it appears that an energy-based method holds the potential for better physical insight into decomposed force terms, and better understanding of highly coupled aerodynamics of integrated airframe propulsion systems.

This work aims to build on the foundation of the underlying concept pioneered by Drela in utilizing the mechanical energy equation to intuitively decompose aircraft aerodynamic forces and powers. To the authors' knowledge the power balance terms have not yet been evaluated explicitly from numerical solutions *. The TASOPT code [27] is based on simplifying assumptions, which allow for volume integrals to be approximated by surface integrals. An example is the thin shear layer assumption, which allows the viscous dissipation within boundary layers to be approximated by surface integrals of defect in kinetic energy[8]. In the authors' opinion, the natural next step in further developing energy-based methods, is to incorporate flow feature spatial identification and extraction to allow for explicit calculation of decomposed terms from numerical solutions, as has been done in momentum-based methods of drag decomposition [2]. To that end, RANS CFD is identified as the appropriate level of modelling fidelity, which also allows for the method to be used within design exploration studies. This paper contributes to the development of energy-based methods through a different approach to applying the mechanical energy equation, where aircraft forces are made to be the subject of the formulation and flow feature extraction is incorporated to allow for physically intuitive force decompositions. Although the proposed approach is generic, and therefore applicable to all forms of propulsion installation, the chosen focus of this work is its application to BLI, as this is considered to represent the most challenging form of airframe-propulsion aerodynamic coupling.

The paper is structured as follows. Firstly, a distinction is made between an absolute versus relative reference frame. As such, the generalised conservation equations of continuity, momentum, mechanical energy and total energy are presented in Section II in both reference frames. Section III details the application of the generalised equations to arbitrary unpowered and powered bodies, in the absolute reference frame, resulting in generic energy-based force decompositions. The advantages of the absolute over the relative reference frame perspective, are argued here.

*By explicitly, it is meant that the mathematical terms from the mechanical energy equation are computed directly from numerical solutions in their original form without any simplifying assumptions. e.g. viscous dissipation is computed from the volume integral definition, and not indirectly from the power balance equation nor from simplified assumptions resulting in surface integrals.

Section IV completes the practical aspect of the decompositions, by introducing volumetric isolation of flow-features, to which the formulations are applied. Finally, the decomposition approach is showcased with an application to BLI in Section V, representing the most extreme aerodynamic coupling between airframe and propulsor. A unique Potential for Energy Recovery metric is introduced to understand and quantify an unpowered body's likely affinity toward BLI. Thereafter, a Design Exploration Study (DSE) of a retrofit, rear-fuselage concentric, BLI propulsor assembly, demonstrates the capabilities of the approach.

II. Conservation Equations in the Absolute Reference Frame

Aircraft aerodynamics are typically assessed in the relative reference frame (RRF), where the aircraft is stationary with flow passing over it. This is convenient in wind-tunnel testing and numerically. However, there are advantages to using the absolute reference frame (ARF) instead, where the aircraft moves through an initially quiescent atmosphere. This enables a more intuitive physical interpretation of mathematical terms, as will become apparent. The transformation between reference frames is based on the velocity relation:

$$\mathbf{V} = \mathbf{V}_A + \mathbf{V}_\infty \quad (1)$$

where \mathbf{V} is the velocity vector relative to the aircraft's frame of reference and \mathbf{V}_A is the absolute velocity vector with reference to earth's axes system conventions [28]. To clarify further, assuming a quiescent atmosphere, $\mathbf{V}_A = 0$ and $\mathbf{V} = \mathbf{V}_\infty$ at a position sufficiently far away from the aircraft such that the flow is not influenced by its presence. This section details the derivation of the conservation equations in both the RRF and then ARF, for an arbitrary closed control volume. First the Mass and Momentum equations are introduced, followed by the mechanical, total and internal energy relations. Finally, it is mentioned here although the equations are generalised, Reynolds averaging considerations may be incorporated as detailed in the Appendix.

A. Mass and Momentum Conservation

Assuming steady conditions, mass and momentum conservation may be written in integral conservation form for an arbitrary control volume of volume \mathcal{V} enclosed by surface \mathcal{S} , as given by Eq. (2) and Eq. (3), respectively [29, 30].

$$\oint_{\mathcal{S}} (\rho \mathbf{V}) \cdot d\mathbf{S} = 0 \quad (2)$$

$$\oint_{\mathcal{S}} \mathbf{V} \rho \mathbf{V} \cdot d\mathbf{S} = \oint_{\mathcal{S}} \left(-p \hat{n} + \bar{\bar{\tau}} \cdot \hat{n} \right) d\mathcal{S} + \iiint_{\mathcal{V}} \rho \mathbf{f} d\mathcal{V} \quad (3)$$

Here ρ and p represent the density and static pressure of the fluid, respectively, and \hat{n} is the unit normal vector along the surface \mathcal{S} , pointing out of the volume \mathcal{V} by convention [29]. $\bar{\bar{\tau}}$ is the viscous stress tensor and is assumed to incorporate

Reynolds Stresses when Reynold Averaging is used, see Appendix. Finally, \mathbf{f} is the net body force per unit mass exerted on the fluid inside the volume \mathcal{V} [29]. Eq. (2) enables Eq. (3) to be rewritten in terms of absolute velocities as given by Eq. (4), and where the substitution of gauge pressure is allowed because \mathcal{S} is closed.

$$\oint_{\mathcal{S}} \mathbf{V}_A \rho \mathbf{V} \cdot \mathbf{dS} = \oint_{\mathcal{S}} \left[-p_G \hat{n} + \bar{\bar{\tau}} \cdot \hat{n} \right] \mathbf{dS} + \iiint_{\mathcal{V}} \rho \mathbf{f} \, d\mathcal{V} \quad (4)$$

B. Mechanical Energy Equation

The mechanical energy balance in conservation differential form is derived from the scalar multiplication between Eq. (3) and \mathbf{V} [7, 31, 32] to give Eq. (5), and is expanded using identities Eqs. (6) and (7) to give Eq. (8).

$$\frac{\partial}{\partial t} \left(\rho \frac{\mathbf{V}^2}{2} \right) + \nabla \cdot \left(\frac{\mathbf{V}^2}{2} \rho \mathbf{V} \right) = -\nabla p \cdot \mathbf{V} + \left(\nabla \cdot \bar{\bar{\tau}} \right) \cdot \mathbf{V} + \rho \mathbf{f} \cdot \mathbf{V} \quad (5)$$

$$\nabla \cdot (p \mathbf{V}) = \nabla p \cdot \mathbf{V} + p \nabla \cdot \mathbf{V} \quad (6)$$

$$\nabla \cdot (\bar{\bar{\tau}} \cdot \mathbf{V}) = \left(\nabla \cdot \bar{\bar{\tau}} \right) \cdot \mathbf{V} + \left(\bar{\bar{\tau}} \cdot \nabla \right) \cdot \mathbf{V} \quad (7)$$

$$\frac{\partial}{\partial t} \left(\rho \frac{\mathbf{V}^2}{2} \right) + \nabla \cdot \left(\frac{\mathbf{V}^2}{2} \rho \mathbf{V} \right) = -\nabla \cdot (p \mathbf{V}) + p \nabla \cdot \mathbf{V} + \nabla \cdot (\bar{\bar{\tau}} \cdot \mathbf{V}) - \left(\bar{\bar{\tau}} \cdot \nabla \right) \cdot \mathbf{V} + \rho \mathbf{f} \cdot \mathbf{V} \quad (8)$$

Applying Eq. (8) to an arbitrary closed control volume, and simplifying via Gauss' Theorem, yields Eq. (9).

$$\frac{\partial}{\partial t} \iiint_{\mathcal{V}} \left(\rho \frac{\mathbf{V}^2}{2} \right) \, d\mathcal{V} + \oint_{\mathcal{S}} \left(\rho \frac{\mathbf{V}^2}{2} \mathbf{V} \right) \cdot \mathbf{dS} = \oint_{\mathcal{S}} \left(-p \mathbf{V} + \bar{\bar{\tau}} \cdot \mathbf{V} \right) \cdot \mathbf{dS} + \iiint_{\mathcal{V}} \left[(p \nabla \cdot \mathbf{V}) - \left(\bar{\bar{\tau}} \cdot \nabla \right) \cdot \mathbf{V} + (\rho \mathbf{f}) \cdot \mathbf{V} \right] \, d\mathcal{V} \quad (9)$$

A final form of Eq. (9) is given by Eq. (10) which assumes steady flow and, following the approach by Drela [7], includes the substitutions $\frac{\mathbf{V}^2}{2} \rightarrow \frac{\mathbf{V}^2}{2} - \frac{\mathbf{V}_{\infty}^2}{2}$ and $p \rightarrow p - p_{\infty} = p_G$ which are permissible because:

$$\frac{\mathbf{V}_{\infty}^2}{2} \oint_{\mathcal{S}} (\rho \mathbf{V}) \cdot \mathbf{dS} = 0, \quad p_{\infty} \iiint_{\mathcal{V}} (\nabla \cdot \mathbf{V}) \, d\mathcal{V} = p_{\infty} \oint_{\mathcal{S}} \mathbf{V} \cdot \mathbf{dS}$$

$$\oint_{\mathcal{S}} \left[\frac{\rho}{2} (\mathbf{V}^2 - \mathbf{V}_{\infty}^2) \mathbf{V} \right] \cdot \mathbf{dS} = \oint_{\mathcal{S}} \left[-p_G \mathbf{V} + \bar{\bar{\tau}} \cdot \mathbf{V} \right] \cdot \mathbf{dS} + \iiint_{\mathcal{V}} \left[p_G \nabla \cdot \mathbf{V} - \left(\bar{\bar{\tau}} \cdot \nabla \right) \cdot \mathbf{V} + (\rho \mathbf{f}) \cdot \mathbf{V} \right] \, d\mathcal{V} \quad (10)$$

Renard and Deck [33] point out that an energy balance analysis in the RRF, i.e. Eq. (10), lacks intuitiveness in external aerodynamic applications, because the power associated with near-field forces is zero due to the no-slip condition at walls i.e. $\mathbf{V} = 0$. Particular reference was made to Drela's Power Balance Formulation [7] in this regard. Subsequently, they demonstrated how a shift to the ARF improved interpretations and insight into the energetic physical mechanisms related to skin friction forces over a flat plate. In a similar vein, this paper takes a different approach to Drela [7]

whereby Eq. (10) is first transformed into the ARF, before applying it to a control volume around an aircraft. Remaining in the ARF from the outset, enables improved understanding into underlying physics behind mathematical terms, when performing a control volume analysis around an aircraft. A transformation of Eq. (10) to the ARF is achieved by first obtaining an expression for the scalar product between the momentum equation and free-stream velocity vector, i.e Eq. (4) $\cdot \mathbf{V}_\infty$. Applying the following identities of Eqs. (11) to (13) yields Eq. (14).

$$[\mathbf{V}_A \rho \mathbf{V} \cdot \hat{n}] \cdot \mathbf{V}_\infty = \frac{\rho}{2} [\mathbf{V}^2 - \mathbf{V}_\infty^2 - \mathbf{V}_A^2] \mathbf{V} \cdot \hat{n} \quad (11)$$

$$\oint_S -p_G \hat{n} \cdot \mathbf{V}_\infty dS = \oint_S -p_G \mathbf{V}_\infty \cdot d\mathbf{S} \quad (12)$$

$$\oint_S (\bar{\tau} \cdot \hat{n}) \cdot \mathbf{V}_\infty dS = \oint_S (\bar{\tau} \cdot \mathbf{V}_\infty) \cdot d\mathbf{S} \quad (13)$$

$$\oint_S \frac{\rho}{2} [(\mathbf{V}^2 - \mathbf{V}_\infty^2) - \mathbf{V}_A^2] \mathbf{V} \cdot d\mathbf{S} = \oint_S [-p_G \mathbf{V}_\infty + (\bar{\tau} \cdot \mathbf{V}_\infty)] \cdot d\mathbf{S} + \iiint_V \rho \mathbf{f} \cdot \mathbf{V}_\infty dV \quad (14)$$

Subtracting Eq. (14) from Eq. (10) gives the final form of the mechanical energy equation in terms of absolute velocities:

$$\oint_S \left[\frac{\rho}{2} \mathbf{V}_A^2 \mathbf{V} \right] \cdot d\mathbf{S} = \oint_S [-p_G \mathbf{V}_A + \bar{\tau} \cdot \mathbf{V}_A] \cdot d\mathbf{S} + \iiint_V [p_G \nabla \cdot \mathbf{V} - (\bar{\tau} \cdot \nabla) \cdot \mathbf{V} + \rho \mathbf{f} \cdot \mathbf{V}_A] dV \quad (15)$$

C. Total and Internal Energy Relations

Eq. (15) only considers mechanical flow powers, and therefore it is necessary to relate it back to the total energy equation. This is primarily important for quantifying the total power used in propelling the aircraft, but is also useful in capturing heat transfer related effects. Where heat transfer effects are significant, further consideration may be given to the second law of thermodynamics, as done in the exergy-based formulations [25]. However, this work makes the tentative assumption that these are negligible, and therefore only the relationship between mechanical and total energy is required. The integral conservation form of the total energy equation [30, 34], applied in the RRF, is:

$$\oint_S \left[\rho \left(e + \frac{\mathbf{V}^2}{2} \right) \mathbf{V} \right] \cdot d\mathbf{S} = \iiint_V \rho (\dot{q} + \mathbf{f} \cdot \mathbf{V}) dV + \oint_S [-\mathbf{q} - p \mathbf{V} + \bar{\tau} \cdot \mathbf{V}] \cdot d\mathbf{S} \quad (16)$$

In Eq. (16) e is the mass specific internal energy, \dot{q} a volumetric heating source term and \mathbf{q} the heat flux due to thermal conduction, which from Fourier's law is proportional to the local temperature gradient via the thermal conductivity coefficient \mathcal{K} , where $\mathbf{q} = -\mathcal{K} \nabla T$ [30]. Subsequently, an expression for internal energy is obtained directly from the first law of thermodynamics [31, 35] or indirectly by subtracting the mechanical energy from the total energy [32, 34],

which in steady flow is given as:

$$\oint_S \rho e \mathbf{V} \cdot \mathbf{dS} = \oint_S -\mathbf{q} \cdot \mathbf{dS} + \iiint_V \left[\rho \dot{q} - p \nabla \cdot \mathbf{V} + \left(\bar{\tau} \cdot \nabla \right) \cdot \mathbf{V} \right] dV \quad (17)$$

The last two integrands in the second term on the right of Eq. (17) are also present in the mechanical energy conservation Eq. (9). This provides additional insight into their physical interpretation where they represent the work done in deforming a fluid element. The latter term $\left(\bar{\tau} \cdot \nabla \right) \cdot \mathbf{V}$ is an increase in internal energy due to viscous dissipation through deviatoric stresses [32, 34] and is equivalent in effect to irreversible heat addition [35]. The former integrand, $-p \nabla \cdot \mathbf{V}$, is due to isotropic stresses and is usually assumed to be reversible [32, 34], where compression or expansion raise or reduce the internal energy respectively. However, Batchelor [35] decomposes it into reversible and irreversible contributions, where the latter is referred to as expansion damping and is due to the mechanical lag between the fluid's equilibrium states. The expansion damping is typically negligible but may be significant in regions containing shocks [35]. It is now convenient to represent the rise in internal energy in the form of Eq. (19), whereby Eq. (2) enables the substitution $e \rightarrow e_\infty$ and through Gauss' theorem the compression work may be expressed with reference to p_∞ :

$$\iiint_V -p \nabla \cdot \mathbf{V} dV = \iiint_V -p_G \nabla \cdot \mathbf{V} dV + \oint_S -p_\infty \mathbf{V} \cdot \mathbf{dS} \quad (18)$$

$$\oint_S \rho (e - e_\infty) \mathbf{V} \cdot \mathbf{dS} = \oint_S (-\mathbf{q} - p_\infty \mathbf{V}) \cdot \mathbf{dS} + \iiint_V \left[\rho \dot{q} - p_G \nabla \cdot \mathbf{V} + \left(\bar{\tau} \cdot \nabla \right) \cdot \mathbf{V} \right] dV \quad (19)$$

Apart from the practical advantage of providing an alternative means for post-processing surface versus volume integrals, Eq. (19) relates some mechanical energy terms back to internal energy, thereby assisting physical interpretations. As identified by Arntz et al. [25], the second term on the right of Eq. (18) is thermodynamically the portion of work done on the surroundings by the system, or visa versa [36]. For an aircraft, it is typically the work done in displacing the atmosphere against its pressure, i.e. p_∞ , and has no presence in the mechanical energy equation as it cannot be used by the system. Instead, because it is unusable, it may be viewed as a loss/expenditure of the system's internal energy. Conversely, the first term on the right of Eq. (18) is found in the mechanical energy equation and, with reference to Eq. (19), may represent either; (1) internal energy expenditure in providing useful work to the system or (2) a waste in available energy within the system resulting in a rise in internal energy. Finally, for completeness, combining Eqs. (15) and (19) yields an expression for the total energy equation in terms of absolute velocities:

$$\oint_S \left[\rho \left(e + \frac{\mathbf{V}_A^2}{2} \right) \mathbf{V} \right] \cdot \mathbf{dS} = \iiint_V \rho (\dot{q} + \mathbf{f} \cdot \mathbf{V}_A) dV + \oint_S \left[-\mathbf{q} - p \mathbf{V}_A + \bar{\tau} \cdot \mathbf{V}_A \right] \cdot \mathbf{dS} \quad (20)$$

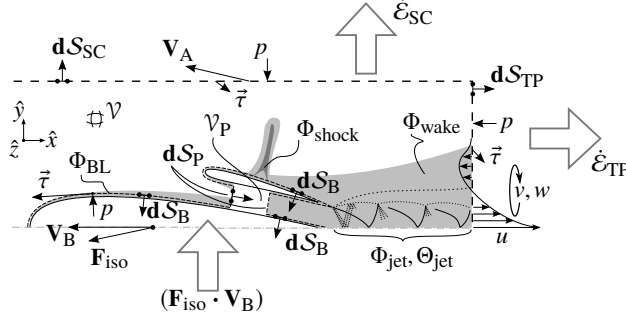


Fig. 1 Control volume around a powered body with work flow paths

III. Force Decompositions

A. Control Volume Description

This section details the force decompositions around an aircraft with the aid of Fig. 1. In a similar approach to Drela [7], this figure shows a single control volume of volume \mathcal{V} , whose near-field surfaces drape the aircraft surfaces S_B and S_P . The former are physical surfaces of the airframe with no mass flux across them, whereas the latter are flux surfaces that are convenient for representing a ducted propulsor that encapsulates an internal volume \mathcal{V}_P . The remainder of the control volume's surfaces are positioned away from the aircraft and collectively referred to as S_O . Assuming a cylinder for S_O , and positioning the upstream surface far ahead within the free-stream flow, allows S_O to be split into a Trefftz plane surface S_{TP} and a side-cylinder surface S_{SC} . By convention the normal vector points outwards along each of these surfaces, as depicted by the surface area vectors dS_B , dS_P , dS_{TP} and dS_{SC} . Forces related to pressure p and shear stresses $\vec{\tau}$ are shown as acting on the control volume, and velocities given in the ARF. The shaded areas depict regions of various flow features such as boundary layers (BLs), shocks, free-shear layers (wake) and jet regions. As these regions are volumetric, they are labelled in the figure using the volumetric viscous dissipation Φ and compression work Θ terms for the purposes of the decomposition description, whereby the contributions of each flow feature to overall Φ and Θ are isolated. These volumetric terms only represent some of the mechanical energy terms, and therefore the large arrows represent energy transfer across the respective boundaries of the control volume, as is discussed further when details of the decomposition are introduced.

Based on the above description, momentum conservation is first used to obtain the aircraft net force from near-field and far-field surfaces. This is useful in identifying the work related to the net force within the mechanical energy equation, and to make it the subject of the energy-based decomposition. Subsequently, the mechanical energy equation is applied to an unpowered body whereby the body is not coupled aerodynamically to a propulsor within the same domain. The unpowered scenario is useful for demonstrating the ARF approach and interpreting the physics behind each mathematical term in the mechanical energy equation. Finally, a powered body is considered, which introduces the additional terms related to the a propulsor coupled aerodynamically to the body.

B. Near and Far-Field Forces from Momentum Conservation

Applying Eq. (4) to a control volume around a powered body, Fig. 1, allows for the net aerodynamic force \mathbf{F}_N to be determined from either near-field integration of shear stresses and pressures along airframe and propulsor surfaces, or alternatively far-field integration of the wake.

$$\begin{aligned}\mathbf{F}_N &= \underbrace{\iint_{S_B} [p_G \hat{n} - \bar{\tau} \cdot \hat{n}] dS}_{\mathbf{F}_B} + \underbrace{\iint_{S_P} [\mathbf{V}_A \rho \mathbf{V} \cdot \hat{n} + p_G \hat{n} - \bar{\tau} \cdot \hat{n}] dS}_{\mathbf{F}_P} - \iiint_{V_P} \rho \mathbf{f} dV \\ &= \iint_{S_0} -[\mathbf{V}_A \rho \mathbf{V} \cdot \hat{n} + p_G \hat{n} - \bar{\tau} \cdot \hat{n}] dS\end{aligned}\quad (21)$$

In Eq. (21) S_B and S_P represent portions of the control volume's surfaces that drape airframe and propulsor, respectively. S_P are flux surfaces, where it is more convenient to capture the change in momentum across the propulsor (e.g. gas turbine engine). Alternatively, a volume integral is required when using force vector field representation of a propulsor, \mathbf{f} . The remainder of the control volume surface encapsulating the aircraft, S_0 , may be positioned far enough ahead, above, below and to the sides of the aircraft, such that the only non-zero terms appear in the Trefftz plane integrations intersecting the aircraft's wake. Theoretically, the Trefftz plane may be positioned at any distance downstream and yield the same net force result. It is this property which allows for net force decompositions into profile, induced and wave drag terms, as carried out in references [1, 2, 4].

In Eq. (21) \mathbf{F}_B is used to denote the integrated skin friction and pressure forces on physical surfaces, whereas \mathbf{F}_P denotes forces associated with flux surfaces or body force volumes that may be introduced to simulate a propulsor[†]. Consideration must be given to the fact that \mathbf{F}_N may be imbalanced, i.e. non-zero. This is certainly the case for an unpowered body where \mathbf{F}_P does not exist and the body is subject to lift and drag forces. It may also be the case for a powered body, whereby the addition of \mathbf{F}_P does not perfectly mitigate \mathbf{F}_B . Such an imbalance would result in acceleration of the body, which does not comply with the steady flow assumption made in Section II. Therefore, a balancing force \mathbf{F}_{iso} is required for static equilibrium, and is assumed to be isolated aerodynamically from the flow-field. As an example, \mathbf{F}_{iso} may represent the weight of an aircraft that opposes lift. Or it may represent the thrust of an engine which opposes the drag of an airframe (or visa versa), when the aerodynamics of the two are considered separately. This concept is useful in describing work flow paths in the following force decompositions.

C. Energy-Based Decompositions of Unpowered Bodies

First, an unpowered body is considered in steady level flight, where there is no change in potential energy due to climb or descent. An unpowered body is defined here as being aerodynamically decoupled from a propulsor, and

[†]It is important to note that \mathbf{F}_B and \mathbf{F}_P are not intended to represent a division between drag and thrust respectively. Instead, they are simply convenient for referring back to the integrals they represent in Eq. (21) and for distinguishing between unpowered and powered configurations, where \mathbf{F}_P represents additional terms due to additional flux surfaces or body forces used to simulate a propulsor.

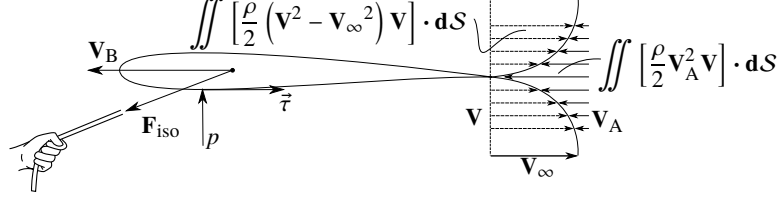


Fig. 2 Unpowered body depicting the comparison between kinetic energy in the relative versus absolute reference frame

therefore without the flux surfaces \mathcal{S}_P shown in Fig. 1, nor does it include any propulsor representative body forces. Following this definition, Eq. (15) is applied to a control volume around an unpowered body and rearranged to give Eq. (22), where \mathcal{S}_O is the outer portion of the control volume surrounding the configuration and, for a front plane positioned far enough ahead of the vehicle, reduces to $\mathcal{S}_O = \mathcal{S}_{SC} + \mathcal{S}_{TP}$, as shown in Fig. 1.

$$\underbrace{\iint_{\mathcal{S}_B} \left[-p_G \mathbf{V}_B + \bar{\tau} \cdot \mathbf{V}_B \right] \cdot d\mathbf{S}}_{-\mathbf{F}_B \cdot \mathbf{V}_B} = \underbrace{\iint_{\mathcal{S}_O} \left[\mathbf{V}_A^2 \frac{\rho}{2} \mathbf{V} + p_G \mathbf{V}_A - \bar{\tau} \cdot \mathbf{V}_A \right] \cdot d\mathbf{S}}_{\dot{\mathcal{E}}_k + \dot{\mathcal{E}}_p + \dot{\mathcal{E}}_\tau} + \underbrace{\iiint_{\mathcal{V}} \left[-p_G \nabla \cdot \mathbf{V} + (\bar{\tau} \cdot \nabla) \cdot \mathbf{V} \right] d\mathcal{V}}_{\Theta + \Phi} \quad (22)$$

The left side of Eq. (22) is described with reference to Fig. 2. As introduced in Section III.B, a balancing force \mathbf{F}_{iso} is required for static equilibrium of the system. \mathbf{F}_{iso} , acting at the flight velocity \mathbf{V}_B , provides the total work input to the system. An analogy may be made with the power applied to a rope pulling the body through the flow[‡]. This work is transferred from the body to the flow via the integrated skin friction and pressure forces acting on the fluid by the body ($-\mathbf{F}_B$). The work transferred at the boundary between the body and fluid, ($-\mathbf{F}_B \cdot \mathbf{V}_B$), is equal to the conventionally defined drag power, ($\mathbf{F}_B \cdot \mathbf{V}_\infty$). Summarising this relationship:

$$\underbrace{\mathbf{F}_{iso} \cdot \mathbf{V}_B}_{\text{total work input to system}} \Rightarrow \underbrace{-\mathbf{F}_B \cdot \mathbf{V}_B}_{\text{work transfer from body's surfaces to fluid}} = \underbrace{\mathbf{F}_B \cdot \mathbf{V}_\infty}_{\text{conventional drag power}} \quad (23)$$

Referring back to the the mechanical energy in the RRF, the first term on the right of Eq. (10) reduces to zero along the boundary between body and fluid, because of the no-slip condition where $\mathbf{V} = 0$. This suggests that no work is done on the flow by the skin friction and pressure forces along its surfaces, which is counter intuitive as this is the only common boundary across which work may be transferred. Conversely, from the ARF perspective, the first term on the right of Eq. (15) readily yields the expected work transfer across this boundary, because the no-slip conditions means that $\mathbf{V}_A = \mathbf{V}_B$. Now, a portion of this work raises the kinetic energy of the fluid in close proximity to the body. From the ARF perspective, the fluid is assumed to be initially stationary ahead of the body. As the body moves through the

[‡]assuming no aerodynamic interaction between the rope and flow-field

air, it comes into immediate contact with some fluid which must accelerate to match the flight velocity, as dictated by the no-slip condition. Due to viscosity, the adjacent fluid regions are pulled along with it, but with diminishing rise in kinetic energy the further away they are from the body. This clear gain in kinetic energy, imparted to the flow by the body, is represented by $\dot{\mathcal{E}}_k$ in Eq. (22) and is readily obtained from the left side of Eq. (15). Conversely, it is unclear what the left side of Eq. (10) really represents, or how to relate it back to the overall work input of the system. It is evident from Fig. 2 that the kinetic energy obtained from the two frames of reference is quite different. However, as explained here, the ARF approach yields an intuitive result, which is easily related back to the initial work transfer across the boundary between fluid and body. An additional advantage of the ARF perspective is that it gives clearer insight into BLI principles, where the kinetic energy imparted to the flow is energy available for utilization by a propulsive device. This is far more intuitive than the RRF perspective, which examines how losses in the a moving atmosphere's kinetic energy may be prevented through wake re-energisation. These two arguments demonstrate how the ARF form of Eq. (15) addresses the previously mentioned concerns of Renard and Deck [33].

Examining further the work transfer from body to fluid, the terms of $\dot{\mathcal{E}}_p$ and $\dot{\mathcal{E}}_\tau$ in Eq. (22) represent the boundary work done on the control volume's flux surfaces due to viscous and pressure forces. Subsequently, because the left of Eq. (22) is constant, work is transferred from $\dot{\mathcal{E}}_k$, $\dot{\mathcal{E}}_p$ and $\dot{\mathcal{E}}_\tau$ to Θ and Φ as the control volume's outer surfaces comprising S_O (i.e. S_{TP} and S_{SC}) are positioned further away from the body. As detailed in Section II.C, this work transfer results in a rise in fluid internal energy through Φ and Θ [§] To further generalise Eq. (22), an excess / deficit in input power in steady flight, not balanced by \mathbf{F}_{iso} , results in climb / decent, respectively. Therefore, similarly to Drela [7], the change in altitude potential energy $(W\dot{h})$ (due to the rate of change in vertical velocity \dot{h}) must be incorporated within Eq. (22) to give:

$$\mathbf{F}_B \cdot \mathbf{V}_\infty = \underbrace{\dot{\mathcal{E}}_k + \dot{\mathcal{E}}_p + \dot{\mathcal{E}}_\tau + \Theta + \Phi}_{\Phi^*} + W\dot{h} \quad (24)$$

It must be noted that Eq. (24) is different from Drela's Power Balance [7] equation, because the ARF terms are different from Drela's RRF terms, and because the work associated with near-field forces has been made the subject of the equation, which lends itself to a force decomposition format. In adopting the notation of Sato [37], the first five terms of Eq. (24) are grouped to represent the aerodynamic power transferred to the control volume, and can now be decomposed to represent the power associated with different flow-mechanisms:

$$\Phi^* = \Phi_{BL}^* + \Phi_{wake}^* + \Phi_{vortex}^* + \Phi_{wave}^* \quad (25)$$

As depicted in Fig. 1, the power input is transferred to Θ and Φ inside the volume, with the remaining power leaving the control volume via the side cylinder S_{SC} and Trefftz plane S_{TP} . The power exiting S_{SC} and S_{TP} are decomposed

[§]Although positive for unpowered cases, Θ may be negative in powered cases.

further, where \mathcal{S}_{SC} is positioned sufficiently far away such that the wake and vortices exit via \mathcal{S}_{TP} only. Given this control volume definition, any remaining energy leaving \mathcal{S}_{SC} is due to the presence of oblique shocks crossing \mathcal{S}_{SC} , and is therefore a portion of the power associated with the shock and also wave drag [7]:

$$\dot{\mathcal{E}}_{SC} = \dot{\mathcal{E}}_{wave} = \iint_{\mathcal{S}_{SC}} \left[\mathbf{V}_A^2 \frac{\rho}{2} \mathbf{V} + p_G \mathbf{V}_A - \bar{\boldsymbol{\tau}} \cdot \mathbf{V}_A \right] \cdot \mathbf{dS} \quad (26)$$

Eq. (27) shows the decomposition of power leaving \mathcal{S}_{TP} , which is divided into components contributing to the profile ($\dot{\mathcal{E}}_{wake}$) and lift-induced ($\dot{\mathcal{E}}_{vortex}$) drag powers, where $\dot{\mathcal{E}}_{vortex}$ is the same as that determined from other decomposition methods [1, 17, 38].

$$\dot{\mathcal{E}}_{TP} = \iint_{\mathcal{S}_{TP}} \underbrace{\left[\frac{\rho}{2} (v^2 + w^2) (u + u_\infty) \right]}_{\dot{\mathcal{E}}_v} + \underbrace{\left[\frac{\rho}{2} u^2 (u + u_\infty) \right]}_{\dot{\mathcal{E}}_a} + \underbrace{\left[p_G u \right]}_{\dot{\mathcal{E}}_p} + \underbrace{\left[(-\tau_{xx}u - \tau_{xy}v - \tau_{xz}w) \right]}_{\dot{\mathcal{E}}_\tau} \mathbf{dS} \quad (27)$$

$\underbrace{\hspace{15em}}_{\dot{\mathcal{E}}_{vortex}} \qquad \underbrace{\hspace{15em}}_{\dot{\mathcal{E}}_{wake}}$

The overall decomposition is completed by determining the contributions of Θ and Φ to each of the terms in Eq. (25). These are calculated by identifying the spatial regions of the flow associated with each flow mechanism, as discussed in Section IV, to which the volume integrals are applied.

D. Energy-Based Decompositions of Powered Bodies

A control volume around a powered body is depicted in Fig. 1, where \mathcal{S}_P coincides with the bounding surfaces of a separate control volume, \mathcal{V}_P , enclosing a generalised propulsor. A set of volumetric body forces may be used to represent the propulsor within \mathcal{V}_P , where the flight velocity power corresponding to the force acting on the propulsor by the fluid is found from Eq. (14) and noting that the normal vector is opposite for the two volumes, i.e. $\mathbf{dS}_P = -\mathbf{dS}_{\mathcal{V}_P}$:

$$\mathbf{F}_P \cdot \mathbf{V}_\infty = - \iiint_{\mathcal{V}_P} \rho \mathbf{f} \cdot \mathbf{V}_\infty d\mathcal{V} = \iint_{\mathcal{S}_P} \frac{\rho}{2} \left[(\mathbf{V}^2 - \mathbf{V}_\infty^2) - \mathbf{V}_A^2 \right] \mathbf{V} \cdot \mathbf{dS} + \iint_{\mathcal{S}_P} \left[p_G \mathbf{V}_\infty - (\bar{\boldsymbol{\tau}} \cdot \mathbf{V}_\infty) \right] \cdot \mathbf{dS} \quad (28)$$

The same result as above is found when applying the same equations to a propulsor with integration over the actual components, instead of using a body force representation. Applying Eq. (15) to the control volume in Fig. 1, and substituting in Eq. (28), yields an expression for the total flight velocity power associated with the body:

$$(\mathbf{F}_B + \mathbf{F}_P) \cdot \mathbf{V}_\infty = \dot{\mathcal{E}}_k + \dot{\mathcal{E}}_p + \dot{\mathcal{E}}_\tau + \dot{\mathcal{E}}_{prop} + \Theta + \Phi + W\dot{h} \quad (29)$$

where the power crossing over from \mathcal{V}_P into the external control volume is given by:

$$\dot{\mathcal{E}}_{\text{prop}} = \iint_{S_P} \left[\frac{\rho}{2} (\mathbf{V}^2 - \mathbf{V}_\infty^2) \mathbf{V} + p_G \mathbf{V} - (\bar{\boldsymbol{\tau}} \cdot \mathbf{V}) \right] \cdot \mathbf{dS} \quad (30)$$

and any imbalance in forces not attributed to a change in altitude, $W\dot{h}$, is accounted for by an isolated force acting on the configuration,

$$\mathbf{F}_{\text{iso}} \cdot \mathbf{V}_B = (\mathbf{F}_B + \mathbf{F}_P) \cdot \mathbf{V}_\infty \quad (31)$$

This derivation is unique in that Eq. (29) allows for a force imbalance in the aerodynamic domain to be accounted for explicitly, which in the authors opinion, is not readily clear from the Power Balance formulation [7]. This is advantageous where it is required to evaluate the performance of a part of an aircraft in isolation from the rest of it. An example would be a BLI fuselage, where it is numerically convenient to model in CFD the fuselage propulsor configuration in absence of the wings and empennage. Any force imbalance on the fuselage-propulsor configuration is balanced by the net force on the remainder of the aircraft's components. As such, it is particularly useful for configurations with a thrust split between BLI propulsors and main podded engines. Eq. (25) is expanded to incorporate the terms related to the jet within the volume \mathcal{V} (but outside of the propulsor volume \mathcal{V}_P) following the definition Eq. (24):

$$\Phi^* = \Phi_{\text{BL}}^* + \Phi_{\text{wake}}^* + \Phi_{\text{vortex}}^* + \Phi_{\text{wave}}^* + \Phi_{\text{jet}}^* \quad (32)$$

Subsequently, Eq. (29), is simplified to:

$$(\mathbf{F}_B + \mathbf{F}_P) \cdot \mathbf{V}_\infty = \Phi^* + \dot{\mathcal{E}}_{\text{prop}} + W\dot{h} \quad (33)$$

If the propulsor is represented by body forces instead of flux surfaces, then the substitution $\dot{\mathcal{E}}_{\text{prop}} \rightarrow (\Theta + \Phi)_{\mathcal{V}_P}$ may be made should \mathcal{V}_P be merged into the overall volume \mathcal{V} .

IV. Flow-Field Feature Extraction

Section III presented decompositions in the combined form of surface and volume integrals. Applying them to CFD results, requires spatial partitioning to isolate flow regions associated with different physical mechanisms. Typically, isolating flow features has been used for qualitative visual representation of the flow, to aid the engineer in improved design. Instead, this paper aims to use such methods so that the aerodynamic power consumption around an aircraft may be appropriately attributed to various flow-features, thus aiding quantification and understanding of integrated airframe and propulsor performance. Steady flow is assumed, as in the case of the previous sections, and flow feature capturing methods considered do not allow for unsteady tracking. Unsteady treatments of drag decompositions are

discussed by Toubin et al. [39].

A. Shear Layers

Convention defines a velocity and thermal BL thickness as the distance normal to the surface at which point the velocity and temperature reach 99% of the BL edge values, respectively. These two thickness' only coincide when the Prandtl number is of unity [40], and it becomes ambiguous to select which is more appropriate. It may be argued that when taking an energy-based approach that the kinetic energy defect defined in Ref [41] is most relevant because of its relation to viscous dissipation in the boundary layer. Nonetheless an additional difficulty is determining the correct edge velocity which will be subject to local flow conditions. Anderson [40] suggests an iterative procedure between inviscid calculations over an effective body and viscous calculations over the real geometry, in order to converge on a displacement thickness and corresponding BL edge conditions. Similarly, Drela [42] describes a series of different Equivalent Inviscid Flow (EIF) models, each increasing in fidelity and complexity, which make use of vortex filaments to mimic the real viscous flow. Although powerful, these approaches are not practical in isolating the BL from RANS CFD solutions over arbitrary bodies. Lovely [43] developed another integral method, which examined vorticity normal to a surface to calculate the momentum thickness directly from viscous RANS CFD data, but it proved to be computationally expensive and impractical for complex flows and geometries [44].

An alternative to integral methods is to use scalar expressions which can be evaluated easily at each cell, to determine to which flow feature that cell belongs. Lovely [43] explored different scalar parameters, including entropy and vorticity, but these measures were found to be shared with other flow features such as shocks. Paparone and Tognaccini [2] employed flow feature extraction within a drag decomposition and quantification scheme, where the shear layer identifier used the local laminar viscosity to normalise the local turbulent viscosity. Although the region identifier is able to omit shocks successfully from coupled regions, it is inherently flawed in that it also excludes the laminar portions of the BLs closest to the wall, which are highly dissipative and required for this type of analysis. Haimes and Kenwright [45] use critical point theory, where eigenvalues of the velocity gradient tensor are combined with local vorticity magnitudes to form a scalar which accounts for the combined effect of vorticity and shear. However, no evidence was given as to the performance of this dimensional scalar, and its ability to omit shocks or other unwanted flow features. Baskett and Haimes [44] later developed a convective approach, whereby a conservation equation is solved iteratively to yield a scalar identifier. The identifier is the subject of a material derivative which, along with a source term, forms an additional flow state equation. This method, reliant on an empirically determined threshold, was very capable of isolating the shear layers in laminar and viscous flow, whilst successfully omitting shocks. Nonetheless, it is complex to implement and, as a conservation equation, is computationally demanding as it requires an iterative solution.

This paper takes a more pragmatic, but still physically relevant, approach whereby ϕ is normalised by the absolute

volumetric pressure work, so as to remove the bulk strain rate contributions typically associated with shocks. This leaves behind dissipation terms only relevant to the shear layers. To reinforce the divide between turbulent shear layers, potential flow and shock regions, the normalised turbulent viscosity is incorporated in the following identifier:

$$\xi = \left(\frac{\mu + \mu_t}{\mu} \right) \left[\frac{(\nabla \cdot \bar{\tau}) \cdot \mathbf{V}}{|\rho \nabla \cdot \mathbf{V}|} \right] \quad (34)$$

This improved identifier now captures laminar zones within the shear layers, due to the very strong dissipation contribution in these regions. A convenient method for calculating an appropriate threshold value for ξ was found to be the volume weighted average of ξ over the whole domain:

$$\xi > \frac{1}{V} \iiint_V \xi \, dV = \frac{1}{V} \sum_{i=1}^n \xi_i \quad (35)$$

where n is the number of cells comprising the entire fluid domain. Eq. (35) is domain dependent, and care should be taken in selecting a sufficiently large domain in obtaining an appropriate threshold. Alternatively, a more rigorous approach is to perform a sensitivity analysis to determine a threshold whereby any further changes in ξ result in a negligible change in Φ_{BL} . Although the above does exclude shocks, it fails to exclude the shock lambda structure present in BL-shock interactions. Appropriately separating this region is governed by a precedence procedure between flow feature filters. In the context of BLI studies, the necessity for separating out shear layer regions is twofold. Firstly, it is of interest to know the quantities of BL ingested, as this is an important variable in parametrically comparing the performance of different configurations. Secondly, it is required to calculate Φ_{BL} within the decomposition formulations.

B. Shockwave Regions

The methods discussed, follow a review on shock wave detection by Ziniu et al. [46], and are also limited to steady flows. Kanamori and Suzuki [47] present a method using characteristic theory, which is able to distinguish between shock, rarefactions and contact discontinuities. One of the claimed advantages is that an empirically derived threshold is not required by the algorithm. Despite these advantages, the method is somewhat complex to implement and, for the sake of pragmatism, other simpler filtering methods were considered to be preferable. Pegendarm and Seitz [48] make use of the density gradient tensor to locate shocks, however the tensor's constituents are not always made available to the user by the CFD solver, and was therefore deemed impractical for this work. Lovely and Haimes [49] developed methods for shock detection in both steady and unsteady flows. In steady flows, the shocks may be located by finding regions where the local Mach number in the direction of the maximum pressure gradient (normal to the shock surface)

is of unity. This is given by Eq. (36) [49].

$$\zeta = \frac{\mathbf{V} \cdot \nabla p}{a|\nabla p|} \quad (36)$$

Spatial pressure gradients are readily an output from most CFD solvers, and this identifier is of practical use. Necessarily, CFD numerically smears shock discontinuities across cells and sufficient mesh refinement is required to capture the shock accurately. However, some degree of smearing is unavoidable for practical meshes and a threshold value is required so as to find the smeared volume appropriately encapsulating the region representing the shock. Paparone and Tognaccini [2] used this identifier in an entropy drag decomposition method, and suggested the use of Rankine-Hugoniot relations to determine an appropriate threshold. However, this is not that simple or practical for complex flows over complex geometries. Instead, Ueno et al. [16] took a more brute-force approach by examining wave-drag versus profile drag sensitivity in response to variations in threshold values, when calculating full-aircraft drag decompositions. However, this process requires manual input and somewhat defeats the objective of automating the decomposition. In lieu of a more accurate approach, this paper assumes that, for an adequately fine mesh, that the shock region is sufficiently captured within 5% of the shock normal Mach, i.e. $\zeta > 0.95$.

C. Jet Region Partitioning

The majority of methods have either focused on flow feature decompositions for unpowered configurations [2, 5] or have not yet tackled jet plume flow feature decomposition [1, 4, 7, 25]. In the absence of significant heat transfer from airframe surfaces, the jet plume represents the only addition of stagnation enthalpy to the flow field. The jet plume volume may be isolated by locating regions where the stagnation enthalpy deviates significantly from the free-stream conditions:

$$\Upsilon = \left| \frac{\Delta H - H_\infty}{H_\infty} \right| > 1.1 \quad (37)$$

where, H_∞ is the total stagnation enthalpy at free-stream conditions, and ΔH the local deviation from this reference value. The inequality of Eq. (37) is useful in that it allows for quantification of the jet plumes contribution to Φ_{jet} and Θ_{jet} . In selecting a threshold value, consideration must be given to stagnation enthalpy profiles within the shear layers. Although there is no net increase in stagnation enthalpy from H_∞ in the adiabatic regions outside of the jet plume, the shear stresses cause a redistribution of H_∞ [50]. Typically the amplitude of H profiles is small in adiabatic conditions, but should the threshold be too close to unity it will filter in localised regions within the boundary layers. Therefore, the threshold value must account for this effect as well as numerical error. $\Upsilon = 1.1$ has been found to be reliable, and in a region where values for Φ_{jet} and Θ_{jet} are insensitive.

Jet flows are complex and it is of interest to further decompose them to isolate relevant internal sub-structures. Such structures have been studied in detail for axisymmetric propulsive jets [51, 52] and more recently for non-axisymmetric underexpanded sonic jets [53], with a review on general jet structures by Franquet [54]. Following these studies, the

primary plume structure may be split into an inviscid core and viscous mixing region. The core region has a plethora of shock and rarefaction wave interactions, which are highly dependent on the degree of underexpansion. Isolating Mach disks, reflected shocks and expansion fans requires very close examination of the flow features. Instead, this work takes a macroscopic approach, and subdivides the core into isentropic expansion and dissipative compression regions. The jet plume is first extracted by applying the filter of Eq. (37). The compression region filter, Eq. (36), is then applied to the plume volume to extract out the compression regions of the core flow. The viscous region filter, Eq. (35) is then applied to the plume volume outside of the core compression regions, which isolates the viscous mixing region of the plume. Having isolated the core compression and viscous mixing regions from the plume volume, leaves behind the remaining volumes of core isentropic expansion.

D. Overall Precedence Procedure

Having extracted the jet plume, leaves behind the remaining volumes of the external flow. It is now necessary to decompose the external flow field into its flow features, including shocks, viscous shear layers and lift induced vortices (this latter decomposition of vortices is not addressed in this paper, and left for a future publication). Separating shocks from shear layers becomes difficult due to the close coupling of boundary layer shock interactions. This work follows the suggestion of Paparone and Tognaccini [2], where the compression region filter takes precedence over the shear layer filter. This precedence allocates the lambda structure within the interaction region to the shock, which allows for a more accurate determination of the dissipation within the shock.

E. A Note on Spurious Effects

In applying volume integrals only to the relevant flow features, any dissipation within the surrounding flow is omitted from the force contributions contained in Φ . This removes any spurious influence on the overall force prediction due to numerically introduced artificial dissipation in the far-field flow [2]. However, artificial dissipation may be excessive within cells very close to the airframe surfaces [4], particularly in areas requiring numerical smoothing because of large flow gradients [1], such as the stagnation zones in the vicinity of the nose cone and wing leading edge [55]. Additional spurious dissipation occurs due to smoothing and oscillations near shock surfaces [1]. Lastly, drag decomposition is affected by artificial dissipation within the lift induced vortices (which far outweighs the physical dissipation), and as such a portion of the induced drag is mistaken for viscous drag [4]. This paper does not address these spurious effects, apart from the omission of far-field numerical dissipation.

V. Application to Boundary Layer Ingestion

BLI has been selected as the demonstrative application for the methods presented in the preceding sections, due to the strong aero-coupling between airframe and propulsor. In this section, RANS CFD studies are first performed

on an unpowered axisymmetric fuselage, representative of a large business jet, prior to inclusion of a BLI propulsor [13]. This not only provides a necessary reference point, but also serves to introduce the concept of an unpowered body's *Potential for Energy Recovery* (PER). Thereafter, design space studies are carried out (in 2D axisymmetric RANS CFD) to explore the potential benefits of retrofitting a rear-fuselage concentric BLI propulsor to the fuselage in a thrust-split configuration.

A. An Unpowered Fuselage

1. Case Description

Fig. 3 illustrates the definitions of the unpowered fuselage geometry, as well as the CFD domain and control volume for post-processing analysis. The fuselage geometry is defined by an overall length $l_{\text{fuse}} = 30m$ and maximum radius $R_{\text{fuse}} = 1.175m$, which is comprised of an elliptical nose of length $l_{\text{nose}} = 3.4R_{\text{fuse}}$, cylindrical mid-body, and tail-cone of length $l_{\text{tail}} = 5.36R_{\text{fuse}}$. The tail-cone is parametrised by a circular arc of radius r_{tail} tangential to the mid-body and right-angled cone with subtended angle $\beta = 20.6^\circ$ at its trailing edge. The CFD domain is 2D axisymmetric about the fuselage's centreline where no angle-of-attack is taken into account. A pressure farfield boundary condition is placed a distance d_{farfield} away from the body, with the wake flowing out of a static pressure outlet boundary condition positioned at a distance d_{outlet} behind the body. The boundary conditions have been set to match flight conditions corresponding to $M = 0.85$ and $Re = 1.26 \times 10^8$. The analysis control volume is defined by a front plane, side cylinder and Trefftz plane placed at distances d_{FP} , d_{SC} and d_{TP} away from the body, respectively. The Appendix contains details of a domain size and grid independence study targeted at eliminating the influence of the boundary condition's presence on \mathbf{F}_B obtained from both Eq. (21) and Eq. (22), whilst also examining sensitivity to boundary layer and wake resolution.

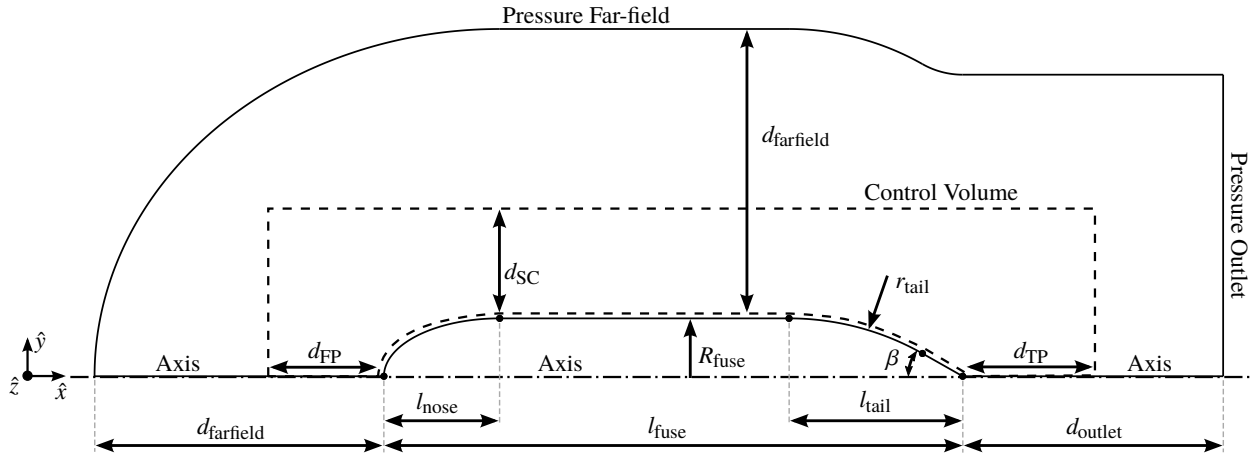


Fig. 3 Definitions of 2D axisymmetric fuselage geometry, CFD domain and analysis control volume.

2. An Unpowered Body's Potential for Energy Recovery

Control volumes with varying Trefftz plane positions behind the fuselage's trailing edge, have been analysed to examine energy transfer pathways between the terms on the right of Eq. (24). Although both sides of Eq. (24) must be constant, the distribution across the five terms on the right will vary at different Trefftz plane positions, as depicted in Fig. 4. At the trailing edge around 90% of the total input power has dissipated irrecoverably to heat within the boundary layers and, in the absence of vortical flows in this non-lifting example, approaches 100% asymptotically as the Trefftz plane is positioned further behind the body. The remaining 10% of the total power input manifests itself in the \dot{E}_k , \dot{E}_p , \dot{E}_τ and Θ terms, and is energy that has not yet been lost irreversibly to the atmosphere. This presents an opportunity for improved aerodynamic performance through strategic integration of a propulsion system, in utilising some of the remaining 10%. This importantly highlights a possible misconception, whereby it may be thought that the ideal BLI potential benefit equates to the streamwise kinetic power imparted to the flow at the trailing edge. This cannot be true since, as observed in Fig. 4, \dot{E}_a equals approximately 45% of the total input power, which exceeds the available 10% remaining after dissipation in the BLs. Instead it is important to consider the transfer between decomposed constituents, whereby the increase in flow kinetic energy is largely balanced by combination of compression work Θ and pressure boundary work potential \dot{E}_p . Based on this concept, a body's potential for aerodynamic improvement may be described by an Potential for Energy Recovery (PER) factor, with S_{TP} defined at its trailing edge:

$$\text{PER} = 1 - \frac{\Phi_{TE}}{\Phi^*} \quad (38)$$

where it may be more useful to exclude all wave power lost to the surroundings:

$$\text{PER} = 1 - \frac{\Phi_{TE} + \dot{E}_{\text{wave}}}{\Phi^*} \quad (39)$$

This is useful in aircraft design because, hypothetically, there may exist two geometrically different bodies with equivalent drag, but different PER values. This could, for example, aid in the design of BLI fuselage shaping prior to the inclusion of the BLI propulsors.

B. Design Exploration Study of a Fuselage Concentric BLI Assembly

1. Design Space Exploration Description

The decomposition methods of Section III have been applied in the analysis of a design-space-exploration (DSE) study, which examined fuselage concentric BLI propulsion concepts in a thrust-split configuration [13]. The thrust-split was defined as the ratio of the net force on the BLI fuselage-propulsor assembly, versus the drag of the entire unpowered aircraft configuration. The remaining deficit in propulsive force, as well as the BLI shaft power, was supplied by two

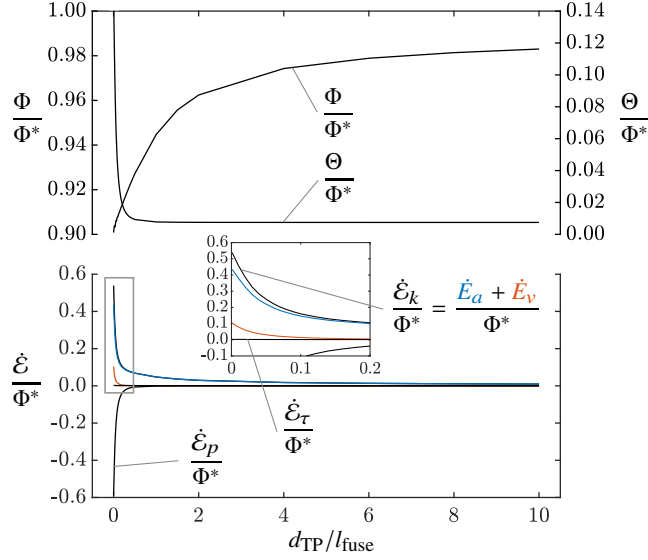


Fig. 4 RANS CFD results of power decomposition transfers with changes in Trefftz plane position behind the trailing edge of a 2D axisymmetric fuselage representation cruising at $M 0.85$ and $Re 1.26 \times 10^8$ [13]

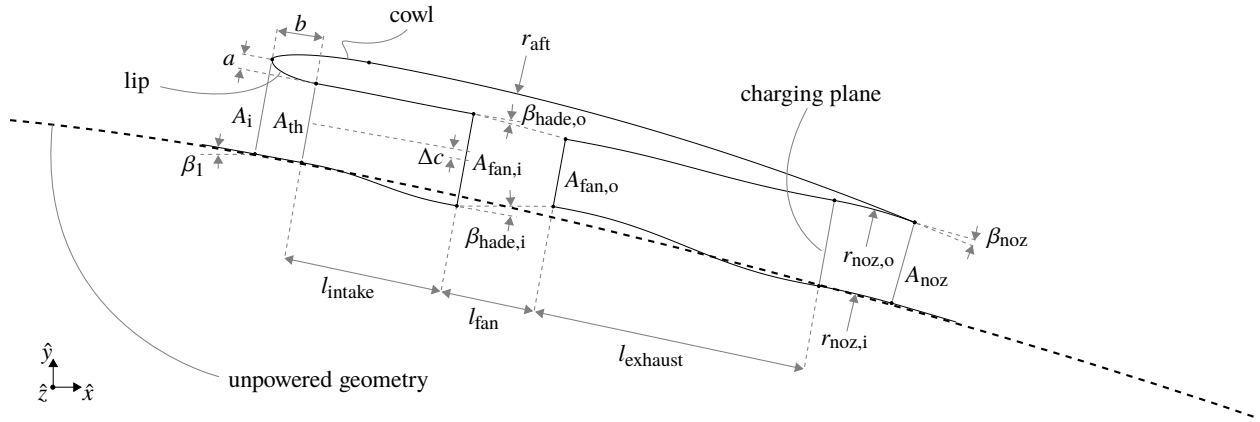


Fig. 5 Definitions of 2D axisymmetric BLI propulsor geometry, which is retrofitted onto the unpowered fuselage geometry

conventional podded turbofans. A retrofit approach was taken, whereby the BLI propulsor conformed to the baseline conventional tail-cone geometry as closely as possible. Definitions of the retrofit geometry are shown in Fig. 5, which is attached to the baseline fuselage and the whole configuration incorporated within a CFD domain similar to that of Fig. 3. The DSE primarily considered variations in thrust-split, Boundary Layer thickness Ratio (BLR) ingested and Fan Pressure Ratio (FPR). The change in net streamwise force of the retrofit BLI fuselage-propulsor assembly from its baseline (unpowered fuselage), was used to compare forces of the different parametric combinations, and is loosely referred to as the Reference Net Assembly Thrust:

$$F_{N_x, \text{ref}} = (F_B + F_P)_{x, \text{powered}} - (F_B)_{x, \text{unpowered}} \quad (40)$$

Assuming the propulsor may be represented as a set of source terms in the momentum and energy equations (i.e. a mass specific vector force field \mathbf{f} and volumetric heating scalar field \dot{q}), the propulsor input power is obtained by rearranging Eq. (16):

$$\dot{W}_P = \iiint_{V_P} \rho (\dot{q} + \mathbf{f} \cdot \mathbf{V}) dV = - \iint_{S_P} \left[\rho \left(e + \frac{\mathbf{V}^2}{2} \right) \mathbf{V} + p \mathbf{V} - \bar{\boldsymbol{\tau}} \cdot \mathbf{V} \right] \cdot \mathbf{dS} \quad (41)$$

The negative sign on the RHS of Eq. (41) follows the unit normal vector definition of S_P in Fig. 1. Subsequently, a non-dimensional ratio of $F_{N_{x,\text{ref}}}$ and \dot{W}_P , allows for comparing the efficacy of each set of parametric combinations:

$$\kappa = - \frac{F_{N_{x,\text{ref}}} \cdot V_\infty}{\dot{W}_P} \quad (42)$$

Eq. (42) should not be mistaken as a replacement for propulsive efficiency, as it is an ill definition for an efficiency because $F_{N_{x,\text{ref}}}$ is a notional concept and not necessarily a correct representation of useful work consumption. However, due to the lack of any better defined metrics, it is useful in the retrofit context of the BLI fuselage-propulsor assembly, because it reveals how much of \dot{W}_P has been used in changing the fuselage streamwise force.

2D axisymmetric RANS CFD in ANSYS Fluent was used to model the flow around the entire retrofitted BLI + fuselage assembly for various parametric combinations. To do so, the solution of the unpowered fuselage was included within a pre-calculation to initialise estimates of the fan boundary conditions and relevant areas along the internal streamtube flow path required to achieve a specified polytropic efficiency and FPR at a given BLR. These estimates were also used to construct the retrofit nacelle, according to some predefined geometric parameters and flow path design constraints. The BLR was pre-determined according to the bare fuselage solution[¶], where its thickness was extracted using Eq. (35). The inlet to the fan, $A_{\text{fan},i}$, was set using a static pressure outlet, with iteration to achieve a specified target mass flow rate corresponding to the BLR calculated from the baseline fuselage flow solution. The fan outlet, $A_{\text{fan},o}$, was represented by a mass-flow inlet, where the total temperature was determined iteratively to target a specific FPR for a given polytropic efficiency.

2. Overall Performance

Results from the 2D axisymmetric CFD studies are summarised in Fig. 6, which depicts κ and thrust-split relations corresponding to various FPR and BLR combinations. The thrust-split was determined from force calculations based on both the energy conservation, Eq. (29), and far-field momentum formulations, Eq. (21), which are indicated by solid and dashed lines in Fig. 6, respectively. As is evident, there are only small discrepancies between the two, which was found to be subject to differences in sensitivity to numerical errors [13]. As expected, the net forward force

[¶]Because the propulsor's presence influences the BL development upstream, this was done to avoid the ambiguity of which position along the fuselage should be selected to be the ingestion plane.

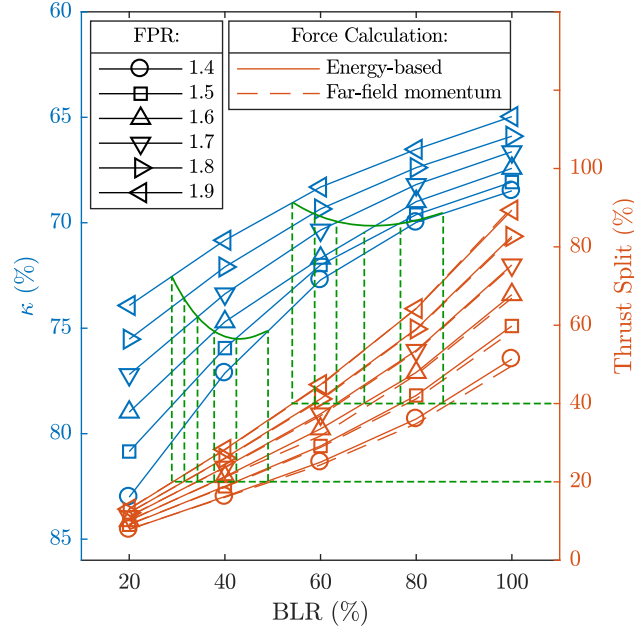


Fig. 6 Parametric performance map of a BLI fuselage-propulsor assembly flying at cruise conditions (Mach 0.85 at an altitude of 45 kft) based on 2D axisymmetric RANS CFD results [13]

on the assembly increases with larger BLRs and FPRs, as more flow is compressed to higher nozzle pressure ratios. The corresponding power consumption is represented within the κ metric, whereby larger values represent better BLI performance and maximums occur at the smallest BLR and FPR combinations. The majority of the kinetic energy imparted to the fuselage BLs (from an ARF perspective) is contained within thin layers closest to the surface, due to the logarithmic shape of the BL's profile. This kinetic energy forms a large proportion of the PER, and subsequently it is most beneficial for the propulsor to act on this thin portion of the BL flow. It is, in fact, the thinnest regions closest to the wall which cause the large wake perturbations within the once quiescent atmosphere, unlike the outer regions of the BLs which are fairly close to the surrounding conditions. Subsequently by ingesting larger BLRs, this outer BL flow is accelerated, thereby adding to the wake perturbation and total energy imparted to the atmosphere, instead of mitigating it. This is exacerbated by larger FPRs, and it is instead more beneficial to operate at lower FPRs where the gross specific thrust at the nozzle exit is minimised. However, operating at such small BLRs and FPRs would not contribute significantly to the overall thrust on the aircraft, and there is additional benefit achievable by distributing the propulsion between the BLI propulsor and main podded turbofan engines. In effect, the BLI propulsor serves to help reduce the jet plume wake from the main podded turbofan engines, and therefore the power transferred to the atmosphere. Therefore thrust-split becomes an important parameter for managing overall propulsion wake attenuation of the aircraft. In this context it can be seen from Fig. 6 that there is an optimum FPR and BLR combination that maximises κ for a given thrust-split. The optimum thrust-split to minimise fuel consumption becomes a balance between κ and the cycle performance and propulsive efficiency of the main podded turbofan engines.

3. Energy Transfers with Trefftz Plane Extent

Having established the overall performance of the BLI assembly configurations, the aerodynamics are analysed further by considering how power is transferred between different energy forms for increasing control volume extents. A coefficient is defined where X may be replaced by any of the surface or volume integrals of Eq. (29) (i.e. $\dot{\mathcal{E}}$, $\dot{\mathcal{E}}$, Θ or Φ):

$$C_X \cdot S_{\text{ref}} = \frac{X}{\frac{1}{2}\rho_{\infty}V_{\infty}^3} \quad (43)$$

Fig. 7 depicts how energy supplied to the air, by the aircraft, is transferred between various forms at different Trefftz plane positions behind the aircraft's trailing edge. This is analogous to the energy content breakdown that a stationary observer would witness changing with time, in the ARF, after the aircraft has flown past. The top three graphs of Fig. 7 indicate how $\dot{\mathcal{E}}_k$ and $\dot{\mathcal{E}}_p$ diminish toward zero, for various combinations of FPR and BLR, as the flow attempts to restore itself to its previous quiescent state^{||}. Correspondingly, the bottom three plots depict the asymptotically cumulative terms of Φ and Θ . Immediately behind the aircraft's trailing edge, within a fraction of a fuselage length, the energy transfer is dominated by rapid exchanges between $\dot{\mathcal{E}}_k$, $\dot{\mathcal{E}}_p$ and Θ , as is evident from the steep slopes. Thereafter, the remaining $\dot{\mathcal{E}}_k$ begins to diminish at a slower rate, which corresponds to the rate at which Φ accumulates. It is concluded that the energy flow path is firstly dominated by resolving Θ , leaving behind a resultant $\dot{\mathcal{E}}_k$, which is subsequently converted to Φ .

An important observation from Fig. 7 is the nonzero cumulative value of Θ . In the power balance method, Drela [7] postulates that Θ is negligible, and only has "strong net contributions at locations wherever heat is added at a pressure far from ambient..." and that "In supersonic wave regions, the integrand may be nonzero, but will cancel when integrated over all points whose streamlines reversibly return to the freestream state...". Although numerical results in Fig. 4 indicate that Θ is negligible for unpowered bodies, the results in Fig. 7 suggest that this may not be an accurate assumption for powered bodies with work introduced in the RRF. As depicted, and with reference to Eq. (43), Θ is found to contribute significantly to forces in the thrust direction. This does seem reasonable when considering the first law of thermodynamics for an open system, i.e. a rearrangement of Eq. (19), which states that the increase in internal energy is equal to combined volumetric pressure work and internal dissipation to heat [31]. Nonetheless, the author was unable to show analytically that Θ is always nonzero, or even if so which force direction it typically contributes to. Therefore it is hypothesised that it is permissible for Θ to be either greater or less than zero, or even exactly zero under special circumstances, but concluded that it should not be assumed to be negligible.

With this understanding in place, it is intuitive that with an increase in BLR and FPR more work is imparted to the flow, and with it the respective values of Θ and Φ where $d_{\text{TP}}/l_{\text{fuse}} \rightarrow \infty$. It is the different balance of these terms for different BLR and FPR combinations, balanced against the input mechanical power $\dot{\mathcal{E}}_{\text{prop}}$, that determines the optimum

^{||} $\dot{\mathcal{E}}_{\tau}$ does too, but is very small in comparison to other terms, and is therefore not shown.

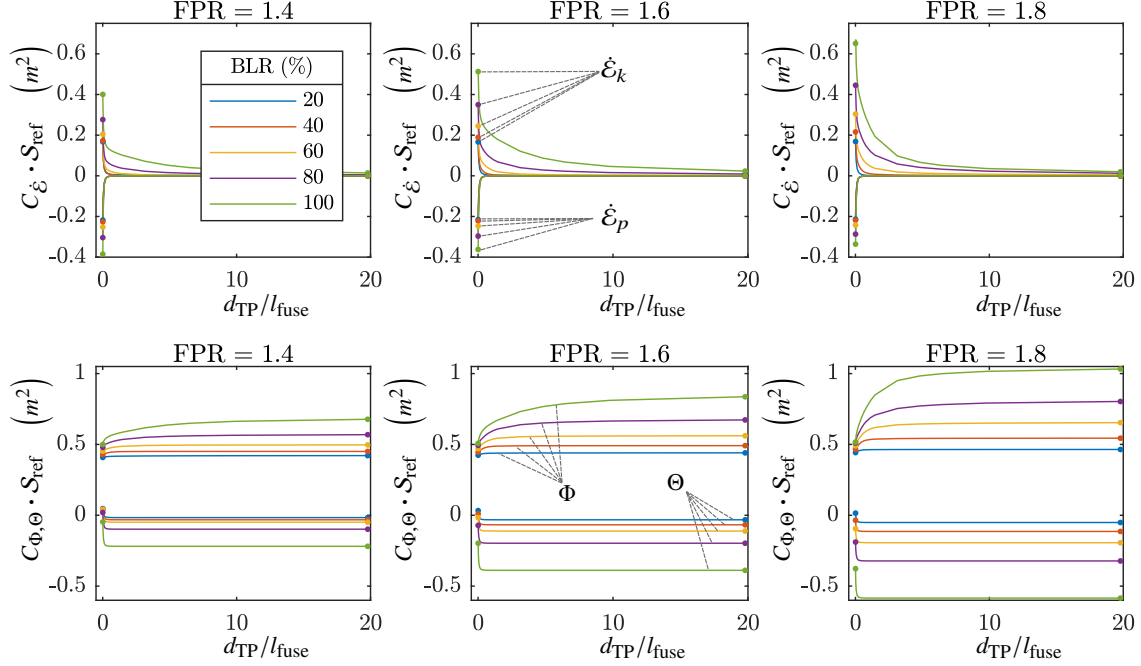


Fig. 7 Energy transfer breakdown with positioning of the Trefftz plane at increasing downstream positions from the aircraft's trailing edge, corresponding to results from Fig. 6

κ for a given assembly force (i.e. thrust split), as shown in Fig. 6. As such, it is of great interest to decompose Θ and Φ into contributions from different flow features, in order to unpack and understand the mechanisms promoting or inhibiting improved integrated aero-propulsive performance.

4. Volumetric Flow Feature Decompositions

Fig. 8 depicts the threshold limits of the filter metrics of Eqs. (34) to (37) applied to the solution of one of the BLR and FPR combinations. This shows how the filters are able to clip out cells, following the precedence procedure detailed Section IV, to extract regions of the flow-field corresponding to different flow features. As shown, Υ nicely separates the jet plume from the external flow, and within it ζ isolates the cells undergoing dissipative compression within the jet core. The oblique shocks and rarefaction waves are seen to reflect off the boundary of the ξ threshold, which is also known as the sonic line within the plume, thus isolating the jet plume viscous mixing region. Remaining behind is the isentropic expansion regions of the jet core depicted by the white contours of ξ , which indicates negligible Φ (and therefore entropy) contributions. The flow external to the jet plume contains a shock which is isolated by the ζ threshold, and can also be seen to correlate with the tight bunching of density contours. Additionally it shows the nacelle submersed within the fuselage's BL, whose boundary is obtained from the ξ threshold and is shown to correspond closely to the traditional $0.99V_e$ definition. ζ is given precedence over ξ and this allows for decoupling of the shock-BL interaction region. Finally, the ξ threshold also divides the BL and free-shear flow from the remaining

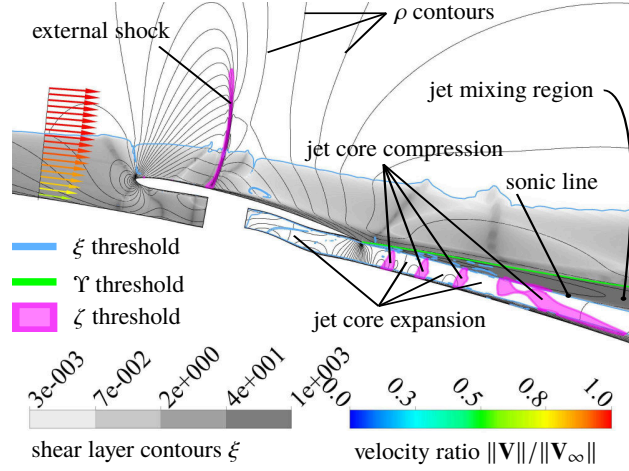


Fig. 8 Flow feature extraction of a BLI numerical RANS solution for the case ingesting BLR 40% and FPR 1.9, indicating threshold boundaries for the filters of Eqs. (34) to (37)

bulk-flow, which is effectively potential flow as seen from the white ξ contours indicating negligible Φ (and therefore entropy). This process of isolating flow features was repeated for all the DSE cases in Fig. 6, to which the volume integrals were applied to quantify each region's contribution to net Θ and Φ . The results are summarised for the separated jet plume and external flow regions in Fig. 9 and Fig. 10, respectively.

Fig. 9(a) and (e) depict C_Φ and C_Θ in the jet core expansion region, respectively. The scatter of negligible magnitude in Fig. 9(a) indicates these regions to be isentropic, whereas the large negative magnitudes of Fig. 9(e) indicate strong expansion and a contribution to forces in the upstream direction. Expectantly, the magnitude of this contribution increases with BLR and FPR. Conversely, the jet core compression region, shown in Fig. 9(b) and (f), exhibits dissipation a couple orders of magnitude greater than the expansion regions. The magnitude is still relatively small, as the flow in this region does not have large shear components. However, the amount of dissipation increases substantially and primarily with FPR, as the internal dissipative shocks increase in strength. A further increase in dissipation correlates to larger BLRs, where larger amounts of mass flow pass through the stronger shock regions. In Fig. 9(f) C_Θ is shown to be relatively small, but positive, indicating that these regions contribute to the net force in the downstream direction. Fig. 9(c) and (g) illustrate contributions of C_Φ and C_Θ , within the jet mixing region. Very large magnitudes of C_Φ are a result of the high shear gradients and turbulent flow, which naturally increases with BLR and FPR. There are also non-negligible negative magnitudes of C_Θ , which illustrates that significant parts of the mixing region is undergoing expansion. Examination of the net values in Fig. 9(d) and (h), shows that dissipation, C_Φ , is dominant in the jet mixing region and that the jet core expansion regions dominate C_Θ . The balance between net C_Φ and C_Θ in (d) and (h), gives the net force contribution of the jet plume. C_Θ far outweighs C_Φ , which leads to the intuitive result that the jet plume has a large overall force contribution in the upstream (thrust) direction. The magnitude of both C_Φ and C_Θ increase with BLR and FPR, however with the former having a greater sensitivity to FPR and the latter a

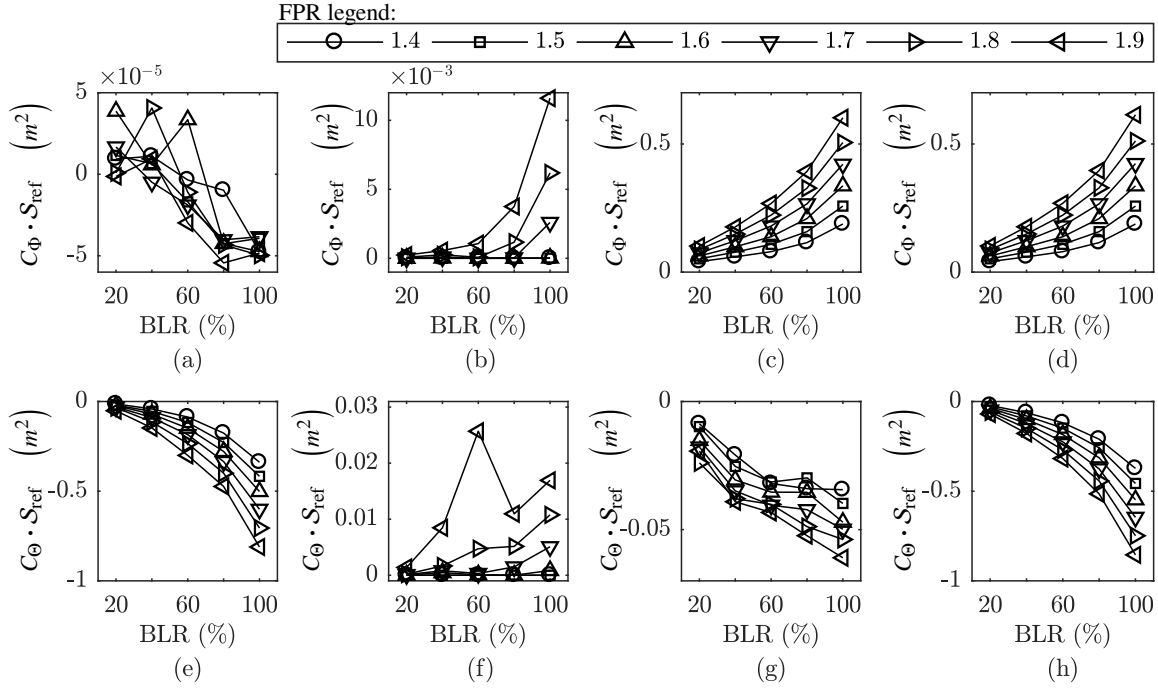


Fig. 9 The (d) net jet plume C_{Φ} comprising contributions from (a) jet core expansion (b) core compression and (c) viscous transition (mixing) regions. The (h) net jet plume C_{Θ} comprising contributions from (e) jet core expansion (f) core compression and (g) viscous transition (mixing) regions.

greater sensitivity to BLR. The ratio between the two, for each BLR and FPR combination, can be viewed as a measure of how effective the jet plume is in producing a thrust force contribution. An optimal balance results in more effective thrust production, but the external flow must also be considered before drawing any further conclusions.

Fig. 10 depicts contributions within different flow regions external to the jet plume. Fig. 10(a) and (e) illustrate C_{Φ} and C_{Θ} in the bulk flow, respectively. This flow is outside of any shear layers or shocks and, having a negligible C_{Φ} contribution, is considered to be regions of potential flow. Contributions to Φ are likely due to errors in threshold values of ξ and ζ . Fig. 10(e) illustrates large expansion contributions to Θ , however this is seen to be largely counteracted by the negative contributions in the shock region shown in Fig. 10(f). This explains the direct correlation with BLR, and insensitivity to FPR, where the external shock is dependent on the intake condition. At smaller BLRs, the nacelle is submersed in the lower Mach regions of the BL, and additionally is a lot smaller meaning that the spilled flow undergoes less acceleration over the cowl. The FPR has only a small influence on the external shock, where the nozzle exit area is smaller for larger FPRs resulting in a slightly stronger shock because of increase cowl and afterbody curvature. Following this reason, and as evident from Fig. 10(b), the shock strength and contribution to Φ increases with BLR. However, the dissipation within the shock is overshadowed by that present in the shear layers of the external flow, Fig. 10(c). But it must be noted that the shock influences the shear layers with which it interacts, with stronger shocks increasingly promoting separation and therefore greater turbulence and dissipation. As such, shear layer dissipation will have a component increasing with shock strength, which correlates to increasing BLRs. Additionally, larger

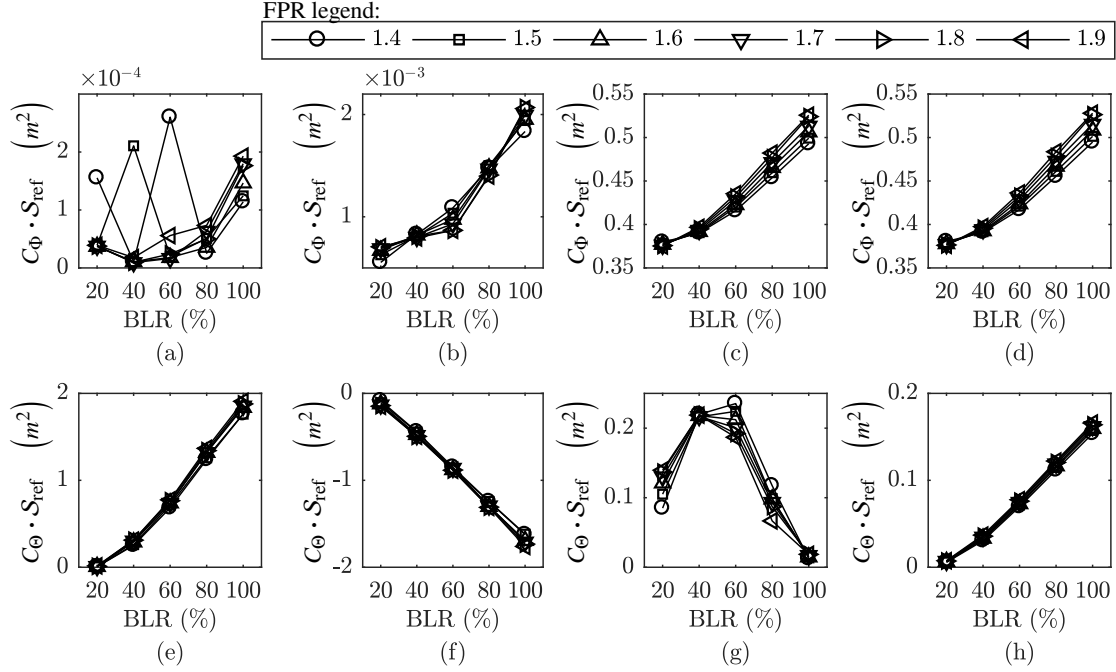


Fig. 10 The (d) net C_Φ external to the jet plume comprising contributions from (a) potential bulk flow (b) external nacelle shock and (c) BL and free-shear regions. The (h) net C_Θ work external to the jet plume comprising contributions from (e) potential bulk flow (f) external nacelle shock and (g) BL and free-shear regions

BLRs have larger nacelles and larger wetted areas with corresponding BLs, which further contributes to the correlation. Furthermore, the shear layer's contribution to Φ will also increase with FPR due to larger gradients within the free-shear layers adjacent to the jet plume mixing region. The net result is that Φ , Fig. 10(d), is mostly due to the shear layer regions, and that it has a correlation dominated by a sensitivity to BLR but with less dominant but significant correlation to FPR. On the other hand Θ , as shown in Fig. 10(h), is quite insensitive to FPR, with a net increase correlating with increases in BLR. In the external flow region, both Φ and Θ net contribution are positive, and thus correspond to a downstream force contribution.

The volumetric breakdowns of Fig. 9 and Fig. 10 have been demonstrated to be extremely useful in unpacking the physics behind the coupled aerodynamics and deciphering correlations to control variables of parametric DSE studies. In examining them, the trends of Fig. 6 can be traced back to the flow mechanisms which influence their shape. The outcome of this is the potential of the proposed energy-based method in aiding strategic design of highly aerodynamically coupled airframe-propulsion systems, by manipulating the respective influence of each flow feature's contributions.

VI. Conclusions

Analysis of highly coupled airframe-propulsion aerodynamics, as in BLI, is challenging because of the difficulty in meaningfully distinguishing between thrust and drag. Subsequently, thrust definitions are no longer able to represent useful work, and propulsive efficiency is no longer a valid metric for assessing propulsive performance. An alternative approach to aircraft aerodynamic analysis is required. This must necessarily include the airframe and propulsor, but only limited insight is achievable through momentum-based control volume analysis. Instead, the mechanical energy equation offers a more detailed, quantifiable and physics-based approach for unpacking aerodynamic interactions. The energy-based formulation presented in this paper builds on the inspired power balance method [7], by taking a different approach of force decompositions. The resulting energy-based method features:

- 1) Generalised formulation of mechanical energy in the absolute reference frame, crucial for intuitive interpretation of physics behind power terms.
- 2) Force decomposition format, instead of *power input = power output*, allowing for an explicit expression of drag for unpowered bodies as well as explicit formulation of force imbalance of powered bodies for evaluation of partial aircraft assemblies in isolation to the rest of the aircraft.
- 3) A novel factor, PER, for quantifying the recoverable wake energy of an unpowered body.
- 4) Flow-field volumetric decomposition method, with filtering metrics allowing for explicit quantification of flow feature contributions to net vehicle force.
- 5) A unique shear layer identifier, which is an improvement on previous identifiers in that it includes laminar portions of the BL close to the wall.
- 6) A precedence procedure for decomposing jet plume and external flow features, and quantifying contributions to overall volumetric dissipation and pressure work.

The formulation was applied to a DSE study of a retrofit rear-fuselage BLI propulsor assembly, with the propulsor concentric to an axisymmetric fuselage. Mapping of the overall results revealed that an optimum, for a given thrust split, exists at a particular BLR and FPR combination. These trends were unpacked by first examining the spatial energy transfer pathways, by considering the wake energy content at various Trefftz plane positions. It was discovered that the volumetric pressure work Θ contributed significantly to forces in the upstream direction and, through examination of volumetric decompositions, were traced back to isentropic expansion regions within the jet core. This is contradictory to works which promote neglecting Θ as a good approximation [7, 8, 10] or add a 5% correction to BL dissipation. This 5% is referenced to Sato [37] who, in fact, found Θ to be 8% of the total mechanical energy loss over a fuselage cruising at M 0.74. From Ref [37], and to the author's knowledge, this 5% correction factor does not appear to be based on empirical data obtained different Mach & Re number combinations, nor a extensive investigation on ducted and unducted propulsors. Therefore, caution should be taken when dealing with contributions from Θ in both magnitude and sign.

Finally, this paper examined how trends of the overall performance map could be traced back to correlations between different flow features and the control variables of the DSE. This demonstrates the proposed energy-based force decomposition formulation, as a useful tool to aid strategic design as well as physics-based understanding of complex highly coupled aero-propulsive flows.

Appendix

Reynolds Averaging Considerations

The implementation of the formulations described in this paper have been performed using Reynolds Averaged Navier-Stokes (RANS) Computation Fluid Dynamics (CFD) simulations, and as such the implications of Reynolds stresses must be accounted for. In its generalised form, the force decomposition assumes that Reynolds stresses are included within the shear-stress tensor $\bar{\bar{\tau}}$, when applied to RANS models. This section of the appendix details the specifics of the Reynolds stress inclusion based on Boussinesq's Approximation, as the results presented in the paper are based on the two-equation, $k - \omega$ SST turbulence model. The rate-of-strain tensors is expressed as [35]:

$$\bar{\bar{S}} = \frac{1}{2} [\nabla \mathbf{V} + (\nabla \mathbf{V})^T] \quad (44)$$

where the superscript T symbolises the transpose of the gradient on velocity tensor. Subsequently, the deviatoric stress is defined [35]:

$$\bar{\bar{d}} = 2\mu \left[\bar{\bar{S}} - \frac{1}{3} (\nabla \cdot \mathbf{V}) \bar{\bar{I}} \right] \quad (45)$$

where μ is the dynamic viscosity, and $\bar{\bar{I}}$ is the identity matrix of equivalent tensor order. Following Eq. (44) and definitions of the Reynolds stress, commonly written in index notation [56], the Reynolds stress tensor may be expressed in the following form so as to avoid reusing symbols already used elsewhere in the paper:

$$\bar{\bar{R}} = 2\mu_t \left[\bar{\bar{S}} - \frac{1}{3} (\nabla \cdot \mathbf{V}) \bar{\bar{I}} \right] - \frac{2}{3} \rho k \bar{\bar{I}} \quad (46)$$

In the above, μ_t is the turbulent or eddy viscosity, ρ is the density and k the turbulent kinetic energy per unit mass. Combining the deviatoric and Reynolds stress of Eqs. (45) and (46), results in the following expression for the shear stress tensor to be applied within the force decomposition method:

$$\bar{\bar{\tau}} = 2(\mu + \mu_t) \left[\bar{\bar{S}} - \frac{1}{3} (\nabla \cdot \mathbf{V}) \bar{\bar{I}} \right] - \frac{2}{3} \rho k \bar{\bar{I}} \quad (47)$$

Eq. (47) may now be used to calculate shear stress forces on surfaces $(\bar{\bar{\tau}} \cdot \hat{n})$ or viscous boundary work $[\bar{\bar{\tau}} \cdot (\mathbf{V} - \mathbf{V}_\infty) \cdot \hat{n}]$. The integrand of the volumetric viscous dissipation, $(\nabla \cdot \bar{\bar{\tau}}) \cdot \mathbf{V}$, may be obtained directly as a result of the shear stress

tensor of Eq. (47). The integrand may be rewritten as the contraction of two second order tensors:

$$\left(\nabla \cdot \bar{\bar{\tau}} \right) \cdot \mathbf{V} = \bar{\bar{\tau}} : \nabla \mathbf{V} = 2(\mu + \mu_t) \left[\bar{\bar{S}} : \nabla \mathbf{V} - \frac{1}{3} (\nabla \cdot \mathbf{V}) \bar{\bar{I}} : \nabla \mathbf{V} \right] - \frac{2}{3} \rho k \bar{\bar{I}} : \nabla \mathbf{V} \quad (48)$$

It may be shown that $\bar{\bar{S}} : \nabla \mathbf{V} = \bar{\bar{S}} : \bar{\bar{S}}$ and $\bar{\bar{I}} : \nabla \mathbf{V} = \nabla \cdot \mathbf{V}$, therefore Eq. (48) becomes

$$\left(\nabla \cdot \bar{\bar{\tau}} \right) \cdot \mathbf{V} = 2(\mu + \mu_t) \left[\bar{\bar{S}} : \bar{\bar{S}} - \frac{1}{3} (\nabla \cdot \mathbf{V})^2 \right] - \frac{2}{3} \rho k (\nabla \cdot \mathbf{V}) \quad (49)$$

Removing the Reynolds stress terms from Eq. (49) yields the viscous dissipation integrand corresponding to the general Navier-Stokes equations, which is found to be the same as that derived by Batchelor [35].

Domain Size and Grid Refinement Study of Unpowered Fuselage

A grid dependence study was conducted alongside a domain size study, and is reported in accordance with the procedures guideline by Celik et al [57]. Grid refinement was focused primarily on regions within the boundary layer and wake, so as to examine the implications of their resolution on the results post-processed using the methods introduced in this work. The domain size was varied to examine sensitivity of the solution to the presence of the far-field and outlet boundary conditions. Three levels of refinement were examined, with their respective refinement regions maintained within three differently sized domains, resulting in a total of nine meshes. The pressure-coupled solver of ANSYS Fluent was used in conjunction with the $k - \omega$ SST turbulence model, and therefore the first wall height of each mesh was maintained such that $y^+ < 1$. With reference to Fig. 3, the selected domain sizes were $d_{\text{farfield}} = 20 \times l_{\text{fuse}}$, $d_{\text{farfield}} = 30 \times l_{\text{fuse}}$ and $d_{\text{farfield}} = 40 \times l_{\text{fuse}}$, with the a corresponding outlet $d_{\text{outlet}} = 3 \times d_{\text{farfield}}$. For convenience, these have been denoted as Domain Size - 20×3 , 30×3 and 40×3 , respectively. To examine BL and wake resolution, mesh refinement was considered for a control volume with the following dimensions: $d_{\text{FP}} = 2 \times l_{\text{fuse}}$, $d_{\text{SC}} = 2 \times l_{\text{fuse}}$ and $d_{\text{TP}} = 50 \times l_{\text{fuse}}$. The results of the study are presented in Table 1, which follows the notation of Celik et al [57]. N_1 , N_2 and N_3 refer to the number of cells within the refinement zone of the CFD domain and correspond to a fine, medium and coarse mesh, respectively. Subsequently, r_{21} and r_{32} , refer to the refinement factor from medium-to-fine and coarse-to-medium, respectively. ϕ_1 , ϕ_2 and ϕ_3 , refer to the force coefficient, for each grid, obtained from Eq. (24), and placed in the form of Eq. (43):

$$\phi = C_{\Phi^*} \cdot S_{\text{ref}} = \frac{\Phi^*}{\frac{1}{2} \rho_{\infty} V_{\infty}^3} \quad (50)$$

Thus ϕ_{ext}^{21} , refers to the Richardson extrapolated value, obtained from an apparent order " p ". Finally, e_a^{21} , e_{ext}^{21} and GCI_{fine}^{21} , refer to the approximate relative error, extrapolated relative error and the fine-grid convergence index, respectively. Table 1 indicates a very close agreement between $C_{\Phi^*} \cdot S_{\text{ref}}$ obtained from the energy formulation of

Table 1 Domain size and grid dependence of net force coefficient obtained from (a) the energy-based formulation of Eq. (22) versus (b) the near-field momentum from Eq. (21) with (c) the difference between the two where applicable.

		Domain Size:								
		(20 × 3)			(30 × 3)			(40 × 3)		
		(a)	(b)	(c)	(a)	(b)	(c)	(a)	(b)	(c)
N_1	(-)	470271	-	-	470037	-	-	470575	-	-
N_2	(-)	268464	-	-	269187	-	-	269477	-	-
N_3	(-)	157987	-	-	157630	-	-	157631	-	-
r_{21}	(-)	1.32	-	-	1.32	-	-	1.32	-	-
r_{32}	(-)	1.31	-	-	1.31	-	-	1.31	-	-
ϕ_1	(m^2)	0.4129	0.4112	0.4%	0.4131	0.4112	0.5%	0.4132	0.4112	0.5%
ϕ_2	(m^2)	0.4147	0.4115	0.8%	0.4151	0.4115	0.9%	0.4153	0.4115	0.9%
ϕ_3	(m^2)	0.4160	0.4115	1.1%	0.4165	0.4114	1.2%	0.4168	0.4114	1.3%
p	(-)	0.90	5.53	-	0.86	4.59	-	0.84	5.41	-
ϕ_{ext}^{21}	(m^2)	0.4081	0.4111	0.7%	0.4079	0.4111	0.8%	0.4075	0.4111	0.9%
e_a^{21}	(%)	0.424	0.080	-	0.468	0.078	-	0.491	0.082	-
e_{ext}^{21}	(%)	1.170	0.022	-	1.288	0.030	-	1.404	0.023	-
GCI_{fine}^{21}	(%)	1.445	0.027	-	1.589	0.038	-	1.731	0.029	-

Eq. (24) versus the near-field value from Eq. (21), which is within 0.5%, 1% and 1.5% for the fine, medium and coarse grids, respectively. This is significant, considering that a Trefftz plane position was selected to be extremely far away from the body, i.e. $d_{TP} = 50 \times l_{fuse}$, for the purposes of the grid convergence study. Furthermore, the numerical uncertainty in the fine-grid solution is less than 2% for all domain sizes, based on the GCI definition. This is despite an apparent order of just under 1, which is considerable given the extent of the control volume analysed, and that Fluent is a second order finite volume solver.

Fig. 11 shows how the GCI varies at different Trefftz plane positions, for all of the grids used. It is immediately evident that with grid refinement, the energy-based force coefficient more closely matches that of the momentum-based near-field results. This is expected, as the finer the mesh, the more accurately it captures the dissipation related to the forces acting on the body. Fig. 11 also shows that the energy-based force coefficient deviates further away from the near-field result, the farther S_{TP} is positioned behind the body. This is due to the accumulative additional dissipation introduced numerically. This spurious addition asymptotes as the wake attenuates to uniform conditions, i.e. where Φ becomes negligible. Finally, it is observed that there is no significant variance between the different domain sizes studied. Further details of these observations are unpacked in Fig. 12, which shows the components of Eq. (24) for each grid and different S_{TP} positions. The first row shows clearly that Φ decreases with finer grids, but increases with d_{TP} as kinetic energy is dissipated. Θ 's cumulative value reaches a constant once the flows' pressure is restored to ambient conditions. However, although small, it is found to decrease with finer meshes, but does still not near zero as is evident

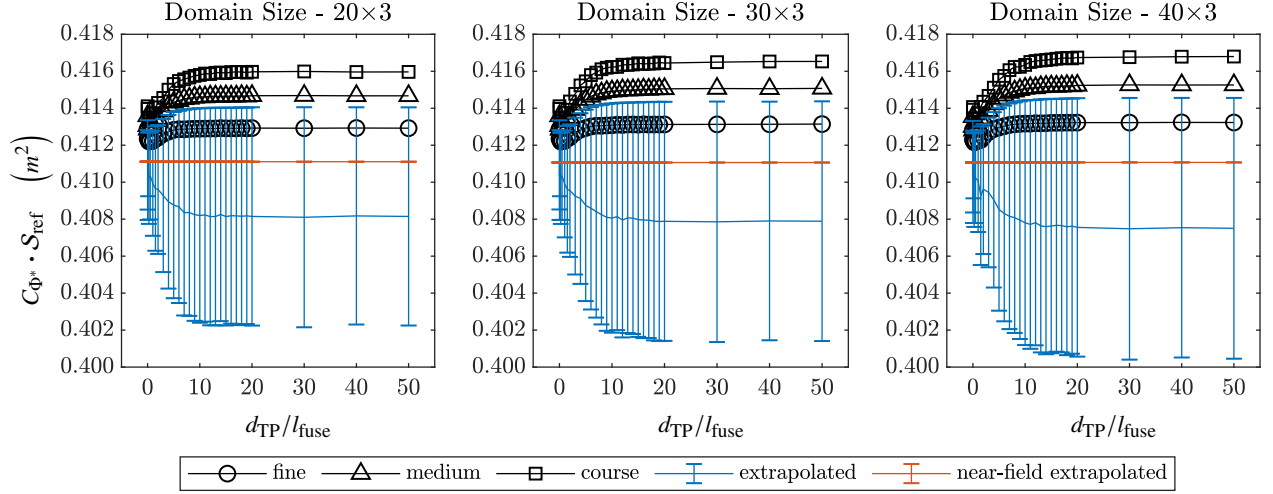


Fig. 11 Grid convergence study: comparison of energy-based force coefficient from Eq. (24) versus momentum-based near-field result from Eq. (21), for different grid refinement and domain sizes.

from the extrapolated values. The kinetic energy $\dot{\mathcal{E}}_k$ and shear stress boundary work $\dot{\mathcal{E}}_\tau$ are almost identical for each grid. This is true for the pressure boundary work $\dot{\mathcal{E}}_p$, despite the larger error bars of GCI, which are a result of the very small values that switch sign around zero, and because of this, the results are not monotonic with mesh density.

Acknowledgments

The authors would like to express their gratitude to Rolls-Royce plc. for supporting this research and for permission to publish the article, with particular thanks to Rory Stieger and Martin Goodhand for their guidance and expertise, without whom this work would not be possible. The authors would also like to thank Lucas Pawsey, Salvatore Ippedico, David John Rajendran and Ioannis Lamprakis, for their respective contributions, insight and advice towards the outcomes of this work. Finally, the work of Mark Drela and his colleagues is acknowledged here, as the inspiration of the theory developed herein, as well as the adoption of the notation and graphic styles used.

References

- [1] Giles, M. B., and Cummings, R. M., “Wake Integration for Three-Dimensional Flowfield Computations: Theoretical Development,” *Journal of Aircraft*, Vol. 36, No. 2, 1999, pp. 357 – 365.
- [2] Paparone, L., and Tognaccini, R., “Computational Fluid Dynamics-Based Drag Prediction and Decomposition,” *AIAA Journal*, Vol. 41, No. 9, 2003, pp. 1647–1657.
- [3] Mele, B., Ostieri, M., and Tognaccini, R., “Aircraft Lift and Drag Decomposition in Transonic Flows,” *Journal of Aircraft*, Vol. 54, No. 5, 2017, pp. 1933–1944. doi:10.2514/1.C034288.
- [4] Destarac, D., and van der Vooren, J., “Drag/Thrust Analysis of Jet-Propelled Transonic Transport Aircraft; Definition of

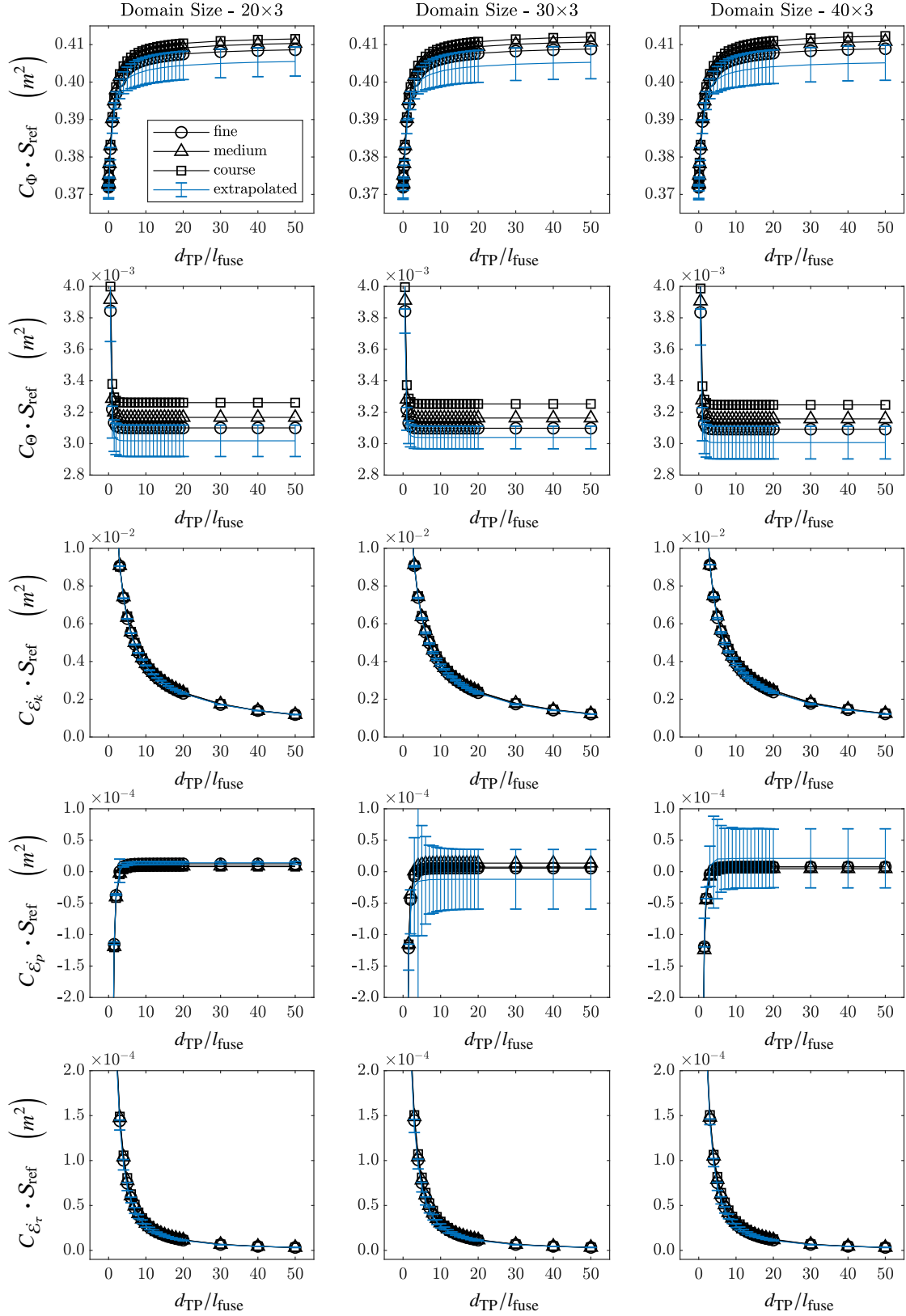


Fig. 12 Grid convergence study: comparison of energy-based force coefficient components of Eq. (24) for different grid refinement and domain sizes.

- Physical Drag Components,” *Aerospace Science and Technology*, Vol. 8, No. 6, 2004, pp. 545–556. doi:10.1016/j.ast.2004.03.004.
- [5] Yamazaki, W., Matsushima, K., and Nakahashi, K., “Drag Prediction, Decomposition and Visualization in Unstructured Mesh CFD Solver of TAS-code,” *International Journal for Numerical Methods in Fluids*, Vol. 57, 2007, pp. 417 – 436. doi:10.1002/fld.1643.
- [6] Yamazaki, W., Matsushima, K., and Nakahashi, K., “Aerodynamic Design Optimization Using the Drag-Decomposition Method,” *AIAA Journal*, Vol. 46, No. 5, 2008, pp. 1096 – 1106. doi:10.2514/1.30342.
- [7] Drela, M., “Power Balance in Aerodynamic Flows,” *AIAA Journal*, Vol. 47, No. 7, 2009, pp. 1761 – 1771. doi:10.2514/1.42409.
- [8] Hall, D. K., Huang, A. C., Uranga, A., Greitzer, E. M., Drela, M., and Sato, S., “Boundary Layer Ingestion Propulsion Benefit for Transport Aircraft,” *Journal of Propulsion and Power*, Vol. 33, No. 5, 2017, pp. 1118 – 1129. doi:10.2514/1.B36321.
- [9] Uranga, A., Drela, M., Greitzer, E. M., Hall, D. K., Titchener, N. A., Lieu, M. K., Siu, N. M., Casses, C., Huang, A. C., Gatlin, G. M., and Hannon, J. A., “Boundary Layer Ingestion Benefit of the D8 Transport Aircraft,” *AIAA Journal*, Vol. 55, No. 11, 2017, pp. 3693–3708. doi:10.2514/1.J055755.
- [10] Uranga, A., Drela, M., Hall, D. K., and Greitzer, E. M., “Analysis of the Aerodynamic Benefit from Boundary Layer Ingestion for Transport Aircraft,” *AIAA Journal*, Vol. 56, No. 11, 2018, pp. 4271–4281. doi:10.2514/1.J056781.
- [11] AGARD, MIDAP Study Group, “Guide to In-Flight Thrust Measurement of Turbojets and Fan Engines,” , January 1979.
- [12] E-33 In Flight Propulsion Measurement Committee, “In-Flight Thrust Determination AIR1730A/B,” SAE International, December 2004.
- [13] Sanders, D. S., “Boundary Layer Ingestion Performance Assessments with Application to Business Jets,” Ph.D. thesis, School of Aerospace, Transport and Manufacturing, Cranfield University, 2018.
- [14] Oswatitsch, K., “Drag and Thrust in Steady Flow,” *Gas Dynamics*, Academic Press, New York, 1956, Chap. 4. General Equations, pp. 207–210.
- [15] Tognaccini, R., “Drag Computation and Breakdown in Power-on Conditions,” *Journal of Aircraft*, Vol. 42, No. 1, 2005, pp. 245–252.
- [16] Ueno, M., Yamamoto, K., Tanaka, K., Murayama, M., and Tognaccini, R., “Far-Field Drag Analysis of NASA Common Research Model Simulation,” *Journal of Aircraft*, Vol. 50, No. 2, 2013, pp. 388–397. doi:10.2514/1.C031766.
- [17] Spalart, P. R., “On the Far Wake and Induced Drag of Aircraft,” *Journal of Fluid Mechanics*, Vol. 603, 2008, pp. 413 – 430.
- [18] Marongiu, C., Tognaccini, R., and Ueno, M., “Lift and Lift-Induced Drag Computation by Lamb Vector Integration,” *AIAA Journal*, Vol. 51, No. 6, 2013, pp. 1420–1430. doi:10.2514/1.J052104.

- [19] Mele, B., and Tognaccini, R., “Aerodynamic force by Lamb vector integrals in compressible flow,” *Phys. Fluids*, Vol. 26, No. 056104, 2014. doi:10.1063/1.4875015.
- [20] Mele, B., Ostieri, M., and Tognaccini, R., “Vorticity Based Breakdown of the Aerodynamic Force in Three-Dimensional Compressible Flows,” *AIAA Journal*, Vol. 54, No. 4, 2016, pp. 1198 – 1208. doi:10.2514/1.J054363.
- [21] Kang, L. L., Russo, L., Tognaccini, R., Wu, J. Z., and Su, W. D., “Aerodynamic Force Breakdown in Reversible and Irreversible Components by Vortex Force Theory,” *AIAA Journal*, Vol. ahead of print, 2019. doi:10.2514/1.J058379.
- [22] Marongiu, C., and Tognaccini, R., “Far-Field Analysis of the Aerodynamic Force by Lamb Vector Integrals,” *AIAA Journal*, Vol. 48, No. 11, 2010, pp. 2543–2555. doi:10.2514/1.J050326.
- [23] Wu, J. C., “Theory for Aerodynamic Force and Moment in Viscous Flows,” *AIAA Journal*, Vol. 19, No. 4, 1981. doi: 10.2514/3.50966.
- [24] Wu, J. Z., Ma, H. Y., and D., Z. M., “Vortical Aerodynamic Force and Moment,” *Vorticity and Vortex Dynamics*, Springer, Berlin, Heidelberg, 2006. doi:10.1007/978-3-540-29028-5_11.
- [25] Arntz, A., Atinault, O., and Merlen, A., “Exergy-Based Formulation for Aircraft Aeropropulsive Performance Assessment: Theoretical Development,” *AIAA Journal*, Vol. 53, No. 6, 2014, pp. 1627–1639. doi:10.2514/1.J053467.
- [26] Hayes, D., Lone, M., Whidborne, J. F., Camberos, J., and Coetzee, E., “Adopting Exergy Analysis for use in Aerospace,” *Progress in Aerospace Sciences*, Vol. 93, 2017, pp. 73–94. doi:10.1016/j.paerosci.2017.07.004.
- [27] Drela, M., “TASOPT 2.00 Transport Aircraft System OPTimization,” Report Cooperative Agreement Number NNX08AW63A, Massachusetts Institute of Technology, March 2010.
- [28] Cook, M. V., “System of axes and notation,” *Flight Dynamics Principles*, Elsevier Aerospace Engineering Series, Elsevier Ltd., 2007, Chap. 2, 2nd ed., pp. 12–14.
- [29] Anderson, J. D., “Aerodynamics: Some Fundamental Principles and Equations,” *Fundamentals of Aerodynamics*, McGraw-Hill Series in Aeronautical and Aerospace Engineering, McGraw-Hill, 2011, Chap. 2, 5th ed., pp. 125–134.
- [30] Anderson, J. D., “The Governing Equations of Fluid Dynamics: Their Derivation, a Discussion of Their Physical Meaning, and a Presentation of Forms Particularly Suitable to CFD,” *Computational Fluid Dynamics; The Basics with Applications*, edited by J. J. Corrigan and E. Castellano, Mechanical Engineering Series, McGraw-Hill International Editions, 1995, Chap. 2, 1st ed., pp. 49–79.
- [31] Schobeiri, M. T., “Differential Balances in Fluid Mechanics,” *Fluid Mechanics for Engineers: A Graduate Textbook*, Springer-Verlag, 2010, pp. 64–66. doi:10.1007/978-3-642-11594-3.
- [32] Kundu, P. K., Cohen, I. M., Ayyaswamy, P. S., and Hu, H. H., “Conservation Laws,” *Fluid Mechanics*, Elsevier Science & Technology, 2010, Chap. 4, 4th ed., pp. 82–137.

- [33] Renard, N., and Deck, S., "A Theoretical Decomposition of Mean Skin Friction Generation into Physical Phenomena Across the Boundary Layer," *Journal of Fluid Mechanics*, Vol. 790, 2016, pp. 339–367. doi:10.1017/jfm.2016.12.
- [34] Aris, R., "Equations of Motion and Energy in Cartesian Coordinates," *Vectors, Tensors and the Basic Equations of Fluid Mechanics*, Dover Publications, INC. New York, 1989, Chap. 6, pp. 120–123.
- [35] Batchelor, G. K., "Equations Governing the Motion of a Fluid," *An Introduction to Fluid Dynamics*, Cambridge Mathematical Library, Cambridge University Press, 2010, Chap. 3, pp. 131–175.
- [36] Cengel, Y. A., and Boles, M. A., "Exergy: A Measure of Work Potential," *Thermodynamics: An Engineering Approach*, McGraw-Hill, 2006, Chap. 8, 5th ed., pp. 423–486.
- [37] Sato, S., "The Power Balance Method for Aerodynamic Performance Assessment," PhD Thesis, Massachusetts Institute of Technology, June 2012.
- [38] Kroo, I., "Drag Due to Lift: Concepts for Prediction and Reduction," *Annual Review of Fluid Mechanics*, Vol. 33, 2001, pp. 587–617. doi:10.1146/annurev.fluid.33.1.587.
- [39] Toubin, H., Bailly, D., and Costes, M., "Improved Unsteady Far-Field Drag Breakdown Method and Application to Complex Cases," *AIAA Journal*, Vol. 54, No. 6, 2016, pp. 1907–1921. doi:10.2514/1.J054756.
- [40] Anderson, J. D., "Introduction to Boundary Layers," *Fundamentals of Aerodynamics*, McGraw-Hill Series in Aeronautical and Aerospace Engineering, McGraw-Hill, 2011, 5th ed., pp. 965–980.
- [41] Drela, M., "Boundary Layer Analysis," *Flight Vehicle Aerodynamics*, The MIT Press, 2014, pp. 57–60.
- [42] Drela, M., "Viscous Effects in Aerodynamic Flows," *Flight Vehicle Aerodynamics*, The MIT Press, 2014, pp. 47–56.
- [43] Lovely, D., "Boundary Layer and Shock Detection in CFD Solutions," MSc Thesis, Massachusetts Institute of Technology, February 2000.
- [44] Baskett, L., and Haimes, R., "Feature Extraction of Shear Layers," *15th AIAA Computational Fluid Dynamics Conference*, 2001. doi:10.2514/6.2001-2665.
- [45] Haimes, R., and Kenwright, D., "On the Velocity Gradient Tensor and Fluid Feature Extraction," *14th Computational Fluid Dynamics Conference*, 1999. doi:10.2514/6.1999-3288.
- [46] Ziniu, W., Yizhe, X., Wenbin, W., and Ruifeng, H., "Review of Shock Wave Detection Method in CFD Post-Processing," *Chinese Journal of Aeronautics*, Vol. 26, No. 3, 2013, pp. 501–213. doi:10.1016/j.cja.2013.05.001.
- [47] Kanamori, M., and Suzuki, K., "Shock Wave Detection Based on the Theory of Characteristics for CFD Results," *20th AIAA Computational Fluid Dynamics Conference*, Honolulu, Hawaii, 2011.

- [48] Pagendarm, H., Seitz, B., and Choudhry, S., “Visualisation of Shock Waves in Hypersonic CFD Solutions,” *Shock Waves @ Marseille I. Springer, Berlin, Heidelberg*, edited by R. Brun and L. Dumitrescu, Springer, Berlin, Heidelberg, 1995, pp. 353–358. doi:10.1007/978-3-642-78829-1_57.
- [49] Lovely, D., and Haimes, R., “Shock Detection from Computational Fluid Dynamics Results,” *14th Computational Fluid Dynamics Conference*, 1999. doi:10.2514/6.1999-3285.
- [50] Drela, M., “Physics of Aerodynamic Flows,” *Flight Vehicle Aerodynamics*, The MIT Press, 2014, pp. 13–14.
- [51] Love, E. S., Grigsby, C. E., Lee, L. P., and Woodling, M. J., “Experimental and Theoretical Studies of Axisymmetric Free Jets,” Technical report, NASA Langley Research Centre, Langley Field, Va, 1959.
- [52] Pao, P. S., and Abdol-Hamid, K. S., “Numerical Simulation of Jet Aerodynamics Using the Three-Dimensional Navier-Stokes Code PAB3D,” NASA Technical Paper 3596, NASA Langely Research Center, Hampton, Virginia 23681-0001, September 1996.
- [53] Menon, N., and Skews, B. W., “Shock Wave Configurations and Flow Structures in Non-Axisymmetric Underexpanded Sonic Jets,” *Shock Waves*, Vol. 20, No. 3, 2010, pp. 175–190. doi:10.1007/s00193-010-0257-z.
- [54] Franquet, E., Perrier, V., Gibout, S., and Bruel, P., “Free underexpanded jets in a quiescent medium: A review,” *Progress in Aerospace Sciences*, Vol. 77, 2015, pp. 25–53.
- [55] Esquieu, S., “Aircraft Drag Extraction from Patched Grid Computations,” *21st Applied Aerodynamics Conference*, Orlando, Florida, 2003.
- [56] Versteeg, H. K., and Malalasekera, W., “Reynolds-averaged Navier-Stokes equations and classical turbulence models,” *An Introduction to Computational Fluid Dynamics: The Finite Volume Method*, Pearson Education Limited, 2007, Chap. 3.7, 2nd ed., pp. 66–97.
- [57] Celik, I. B., Ghia, U., Roache, P. J., Freitas, C. J., Coleman, H., and Raad, P. E., “Procedure for Estimation and Reporting of Uncertainty Due to Discretization in CFD Applications,” *ASME Journal of Fluids Engineering*, Vol. 130, No. 7, 2008. doi:10.1115/1.2960953, URL <https://doi.org/10.1115/1.2960953>.

Full-aircraft energy-based force decomposition applied to boundary layer ingestion

Sanders, Drewan S.

2020-10

Attribution-NonCommercial 4.0 International

Sanders DS, Laskaridis P. (2020) Full-aircraft energy-based force decomposition applied to boundary layer ingestion. AIAA Journal, Volume 58, Issue 10, October 2020, Article number J058695

<https://doi.org/10.2514/1.J058695>

Downloaded from CERES Research Repository, Cranfield University